Medical Oncology (2025) 42:414
https://doi.org/10.1007/s12032-025-02977-x

ORIGINAL PAPER

Next-generation nanoformulation: *Glycyrrhiza glabra*-based chitosan–curcumin MgO/Fe_2O_3 nanocomposite for targeted lung cancer therapy with dual antioxidant action

Alaa Elmetwalli[1] · Sara Abdelsayed[2] · Ashraf Elsayed[3] · Mohammed S. El-Hersh[4] · Mervat G. Hassan[2] · Lamia A. Gad[5] · Medhat Ali Salah[6] · Mohamed Basiouny Yahia[6] · Mohamed A. Shaheen[6] · Mohamed F. Ibrahim[6] · Abdullah Mustafa Ibrahim[6] · Hatem Mohamed Newish[7] · Eman Alhomaidi[8] · Ali H. El-Far[9] · Khaled M. Elattar[10]

Received: 26 May 2025 / Accepted: 29 July 2025

Abstract

This study aims to develop and evaluate *Glycyrrhiza glabra*-based magnesium oxide/iron oxide nanocomposite (NC) functionalized with chitosan and curcumin to enhance therapeutic efficacy against lung cancer and oxidative stress. This is the first report integrating *G. glabra* extract with chitosan and curcumin functionalization into a MgO/Fe_2O_3 nanocomposite for enhanced antioxidant and anticancer effects. The developed nanocomposite demonstrated strong biocompatibility and in vitro therapeutic efficacy, as evidenced by low cytotoxicity in normal cells and significant inhibitory effects against A549 lung cancer cells. In this study, bioactive phytochemical-loaded *G. glabra* extract was used as a green capping and reducing agent to synthesize MgO/Fe_2O_3 NC. The nanomaterials were also functionalized with curcumin and chitosan to promote stability, bioavailability, and site-specific pharmacological activity. The synthesis process was carried out under green conditions, in which the nanocomposite was characterized using FTIR, UV–Vis spectroscopy, EDX analysis, zeta potential analysis, HR-TEM, and XRD. The antioxidant potential was assessed through the DPPH free radical scavenging activity, whereby MgO/Fe_2O_3–chitosan–curcumin NCs yielded the maximum inhibition of free radicals ($IC_{50} = 0.0977$ mg/mL) when compared to other nanomaterials. Antimicrobial activity was assessed against Gram-negative and Gram-positive bacteria, wherein MgO/Fe_2O_3 NC showed moderate activity, and chitosan and curcumin functionalization reduced this to some extent by possibly controlled release behavior or protection of active sites. Cytotoxicity against A549 human lung cancer cells showed strong inhibition by the MgO/Fe_2O_3–chitosan–curcumin NC ($IC_{50} = 10$ µg/mL), confirmed by changes in morphology in accordance with apoptosis. In addition, in silico ADME simulation suggested favorable bioavailability and low toxicity, which is an indicator of the therapeutic potential of these NCs. To the best of our knowledge, this is the first report on *G. glabra*-mediated green synthesis with dual functionalization of chitosan and curcumin in a MgO/Fe_2O_3 nanocomposite. The formulation has synergistic antioxidant and anticancer activity with vast potential in lung cancer therapy. As a whole, the findings address the dual antioxidant and anticancer properties of *G. glabra*-derived MgO/Fe_2O_3–chitosan–curcumin NC and their green potential as agents in the treatment of lung cancer. In vivo studies are recommended to confirm efficacy and safety.

Keywords *Glycyrrhiza glabra* · Green synthesis · MgO/Fe_2O_3–chitosan–curcumin NC · Antioxidant activity · Antimicrobial activity · Anticancer activity

Abbreviations

ADME	Absorption, distribution, metabolism, and excretion
BBB	Blood–brain barrier
CI	Combination index
DMEM	Dulbecco's modified eagle medium
DMSO	Dimethyl sulfoxide
DPPH	2,2-Diphenyl-1-picrylhydrazyl
DRI	Dose reduction index
EDX	Energy-dispersive X-ray spectroscopy
Eg	Bandgap energy
FBS	Fetal bovine serum
Fe_2O_3	Iron(III) oxide
FTIR	Fourier transform infrared spectroscopy
GI	Gastrointestinal
HR-TEM	High-resolution transmission electron microscopy

Extended author information available on the last page of the article

Published online: 07 August 2025

IC_{50}	Half-maximal inhibitory concentration
MgO	Magnesium oxide
MTT	3-(4,5-Dimethylthiazol-2-yl)-2,5-diphenyl tetrazolium bromide
NC	Nanocomposite
NPs	Nanoparticles
SEM	Scanning electron microscopy
UV–Vis	Ultraviolet–visible spectroscopy
XRD	X-ray diffraction

Introduction

Natural plants have gained enormous scientific attention due to their rich content of bioactive molecules and their sustainable and safe use in traditional medications. Due to their multifaceted applications, these plants are progressively required in several industries, including medicine, food, cosmetics, and pharmaceuticals. The Fabaceae family's *Glycyrrhiza glabra* (Licorice) has been highly valued for hundreds of years as a result of its medicinally useful properties. It is a gold mine for phytochemicals such as glabrin A and B, isoflavones, 18β-glycyrrhetinic acid, and glycyrrhizin with reported antibacterial, antiviral, antioxidant, anti-inflammatory, and anti-diabetic activity [1]. *G. glabra* root has also been used in the form of extract, which is a highly regular drink, and tooth powder [2]. It is commercially used in the production of sweeteners and flavoring [3]. Furthermore, Licorice is also nutritionally robust and consists of proteins, amino acids, trace elements like zinc, iron, and selenium, and bioactive compounds like flavonoids and saponins, thereby being therapeutically heterogeneous [4, 5].

Nanotechnology transformed modern science and brought innovations to a variety of branches, ranging from medicine to energy and material science. Due to their large surface area-to-volume ratio, nanoparticles (NPs) possess dramatic physicochemical characteristics that render them highly useful in a wide variety of applications, especially antibacterial and anticancer therapy [6]. Among NPs, metal oxide varieties such as MgO and Fe_2O_3 stand out due to their stability, biocompatibility, and tunable functionalities [7]. These NPs have shown exceptional promise in targeted drug delivery systems, enabling selective binding to tumor receptors and facilitating controlled release of therapeutic agents [8, 9].

Green nanotechnology is a sustainable and eco-friendly method for the synthesis of NPs. Plant extracts are utilized in the synthesis of NPs, which is an integral part of this strategy as it minimizes the use of harmful chemicals and energy-requiring methods. Plant-assisted synthesis exploits phytochemicals in natural extracts to reduce and stabilize metal ions, and create NPs that are enhanced in bioactivity and biocompatibility [10–13]. *Glycyrrhiza* species have been successfully utilized in NPs synthesis. *G. uralensis*, for instance, was utilized to synthesize manganese oxide NPs with anticancer properties [14], and *G. glabra* extract has made it possible to synthesize iron oxide NPs, improving biofortification of crops [15–18]. The findings indicate that Glycyrrhiza-mediated NPs' diversity of applications has been exemplified in biomedical and agricultural fields. Another cornerstone of this work is curcumin, a bioactive turmeric-derived molecule.

Widely known for its extensive anti-inflammatory, antioxidant, and anticancer properties, curcumin has been an integral component of traditional medicine [19].

However, its therapeutic ability has also been significantly enhanced by the development of nanobiotechnology. Curcumin-loaded nanoparticles show increased solubility, stability, and bioavailability and are therefore of the highest importance for the treatment of a variety of diseases [20]. Curcumin-functionalized metal NPs have further enhanced the efficacy of curcumin by allowing improved drug delivery and targeted killing of cancer cells. For example, gold NP-conjugated curcumin displayed great cytotoxic activity against prostate cancer cells [21, 22], while polymeric NPs of curcumin have been able to permeate the blood–brain barrier and have been shown to be promising brain cancer treatments [23]. Although extensive research work has been conducted on the isolated use of *Glycyrrhiza glabra*, curcumin, and metal oxide nanoparticles, it is a significant unknown so far to comprehend their synergistic activity when blended into a single combined nanocomposite system. Most of the work performed so far is confined to isolated species, ignoring the increased therapeutic effectiveness that would be achieved through their combination. Overcoming this shortcoming, this work attempts to synthesize and comprehensively characterize a novel *G. glabra*-mediated MgO/Fe_2O_3 chitosan- and curcumin-functionalized nanocomposite. In one nanoformulation, such multifunctional therapeutic functionalities as antioxidant, antibacterial, and anticancer, particularly for targeted lung cancer therapy, are designed.

To our knowledge, this is the first such report that employs a plant-mediated green synthesis of *G. glabra* in combination with dual biopolymer and phytochemical functionalization in a MgO/Fe_2O_3 matrix. This three-component strategy generates double therapeutic impact, low-cost, scalable, improved biocompatibility, nontoxic material, and eco-friendly synthesis, a very encouraging advancement in green nanomedicine.

Materials and methods

Reagents and chemicals

All chemicals and reagents used in this study were of analytical grade and used without further purification unless

otherwise stated. Dried *G. glabra* root powder was obtained from a local market in Mansoura, Egypt. Magnesium sulfate ($MgSO_4$, ≥ 98%), ferric sulfate ($Fe_2(SO_4)_3$, ≥ 98%), chitosan (medium molecular weight, ≥ 75% deacetylated), curcumin (≥ 94% purity), ethanol (analytical grade, 80%), dimethyl sulfoxide (DMSO, ≥ 99.9%), and all other solvents were purchased from Sigma-Aldrich (St. Louis, MO, USA). Cell culture reagents including Dulbecco's Modified Eagle Medium (DMEM, Cat# 11965092), fetal bovine serum (FBS, Cat# 16000044), penicillin–streptomycin (100 U/mL and 100 µg/mL, Cat# 15140122), and MTT reagent (Cat# M6494) were procured from Thermo Fisher Scientific (Waltham, MA, USA). Ultrapure deionized water was used throughout all experiments.

Preparation of *G. glabra* extract

Dry roots of *G. glabra* were purchased from Mansoura local herbal market, Egypt (Latitude: 31.0364° N, Longitude: 31.3807°E). Plant material was taxonomically authenticated and certified by a plant taxonomist, Faculty of Science, Botany Department, Mansoura University. 10 g of the dried root material was carefully weighed and transferred into a 250 mL conical flask. 100 mL of 80% (v/v) ethanol prepared from analytical grade ethanol and deionized water was added. The flask was placed in a water bath shaker and continuously agitated at 200 rpm at 25 ± 2 °C for 2 h for the extraction of phytochemicals. After agitation, the mixture was allowed to stand overnight (approximately 16 h) at room temperature for maximum extraction yield. The mixture was then filtered to remove the residual plant materials. The resulting filtrate was collected and stored in amber glass bottles to protect it from light degradation and refrigerated at 5 °C until further use in synthesis and analysis [24].

Green synthesis of nanomaterials

Green synthesis of MgO/Fe_2O_3 NC

MgO/Fe_2O_3 NC green synthesis was performed using an eco-friendly, sustainable approach based on the utilization of *G. glabra* extract as a capping and reducing agent. Magnesium sulfate (0.1 M, 50 mL) and ferric sulfate (0.1 M, 50 mL) stock solutions were also separately prepared by dissolution of respective salts in deionized water under stirring until complete dissolution. 50 mL of *G. glabra* extract (16.42 mg/mL) was added dropwise to a stirred solution of magnesium sulfate solution under constant stirring at 25 °C. Next, another 50 mL aliquot of *G. glabra* extract was also added dropwise to the ferric sulfate solution while stirring continuously. The plant extract acted both as a reducing agent, facilitating the reduction of metal ions (Ag^+ and Fe^{3+}) to metallic NPs (Mg and Fe NPs), and as a capping agent, stabilizing the NPs formed. Both mixtures were then heated to 60 °C gradually and stirred for 1 h continuously, until a clear color change was noticed in both mixtures owing to the metal NPs formation. After NPs formation, the solution of magnesium NPs was added slowly portion-wise to ferric oxide NPs suspension under strong stirring to initiate MgO/Fe_2O_3 NC formation. The pH of the mixture was adjusted carefully to 8.5 by adding 0.1 M sodium hydroxide (NaOH) solution to obtain stabilized NC. The resulting mixture was stirred further for 3 h at 60 °C for complete interaction and composite structure formation. To favor the NC formation and prevent agglomeration, the suspension was sonicated for 1 h at 60 °C using an ultrasonic bath [25]. Solid NPs were recovered after synthesis by centrifugation at 10,000 rpm for 15 min, washed repeatedly with 80% ethanol to remove residual impurities and unreacted precursors, and dried in an oven at 60 °C for 24 h. Dried NC powder was then further characterized by FTIR, SEM, EDX, and XRD analyses.

Preparation of MgO/Fe_2O_3/Chitosan NC

A solution of chitosan was prepared by dissolving chitosan powder of concentration 1% w/v in 1% (v/v) acetic acid solution under continuous stirring at room temperature until a homogeneous and clear solution was obtained. 100 mg of prepared MgO/Fe_2O_3 NC was gradually added to the solution of chitosan under vigorous stirring to achieve uniform dispersion of NPs in the polymer matrix. The resulting mixture was stirred at 60 °C for 2 h to obtain effective interaction and bonding between the polymer chains of chitosan and NPs. It also serves to coat NPs with chitosan to increase stability and biocompatibility. The suspension was centrifuged following stirring at 10,000 rpm for 15 min to separate the solid NC from the supernatant. The solid was then extensively rinsed a number of times using 70% ethanol to desorb any loosely bound chitosan or remaining impurities. The clean NC was then dried in a hot air oven at 60 °C for 24 h to obtain a dry powder for later use and characterization [26].

Preparation of MgO/Fe_2O_3–chitosan NC–curcumin

Curcumin (5 mg/mL in ethanol) was subsequently added to the previously dispersed MgO/Fe_2O_3–chitosan NC suspension under stirring conditions (~ 25 °C). The mixture was stirred for 3 h to permit curcumin molecules to adsorb onto and incorporate within the NC matrix effectively. The mixture, after the stirring period, was sonicated for 2 h at 60 °C using an ultrasonic bath to enhance even dispersion of curcumin into the NC, prevent aggregation, and enhance final curcumin-loaded NC stability [27].

Chemical characterization of NC

A series of complementary analytical instruments analyzed the synthesized MgO/Fe2O3 NC and the derived nanomaterials to confirm their structure, morphology, and chemical composition. UV–Visible spectroscopy (Shimadzu UV-2600, Kyoto, Japan) was first used to monitor the optical characteristics and evolution of the NC. Absorption spectra between the 200–800 nm wavelength range were recorded, with metal oxide nanoparticle characteristic peaks. Fourier Transform Infrared (FTIR) (Waltham, MA, USA) spectroscopy was performed to identify the functional groups accountable for the reduction and capping process and to identify the presence of chitosan and curcumin on the NC surface. Energy Dispersive X-ray (EDX) (Billerica, MA, USA) spectroscopy coupled with Scanning Electron Microscopy (SEM) was employed for the examination of the surface topography and morphology of NC. The samples were drop-cast from suspensions of the NPs on conductive substrates and subsequently covered with a thin layer of gold for conductivity enhancement. Imaging was performed at various magnifications using a SEM device (JEOL JSM-6510LV, JEOL Ltd., Tokyo, Japan) with a typical accelerating voltage of 10–20 kV [28]. HR-TEM (JEOL JEM-2100, JEOL Ltd., Tokyo, Japan) was applied to analyze the size, shape, and morphology of the NPs at the nanoscale. Samples were prepared by suspending nanoparticle suspensions drops onto carbon-coated copper grids, enabling the visualization of their nanoscale structures in detail. X-ray Diffraction (XRD) (Billerica, MA, USA) analysis ultimately confirmed the crystallinity as well as phase purity of the NC. Using Cu Kα radiation ($\lambda = 1.5406$ Å), diffraction patterns were recorded in a 2θ range of 10°–80° and compared with standard reference data to identify the crystalline phases formed. Measurements of zeta potential were made to assess the colloidal stability and charge on the surface, which are crucial in forecasting the dispersion behavior and stability of the NC in water under aqueous conditions that are essential to their biological applications [29, 30].

Phytochemical analysis

The total phenolic content of the plant extract and synthesized nanomaterials was determined using the Folin-Ciocalteu (F–C) assay [31, 32]. This method treated the extract and nanomaterials with Folin-Ciocalteu reagent, forming a blue-colored complex. The intensity of this color, indicative of phenolic concentration, was measured using a spectrophotometer. The phenolic content was quantified using a gallic acid standard curve ($y = 0.0062x$, $R^2 = 0.987$). The aluminum chloride colorimetric method was employed to assess the total flavonoid content [33, 34]. The reaction between aluminum chloride and flavonoids generates a red-colored complex, the intensity of which was also measured spectrophotometrically. The flavonoid content was expressed as milligrams of catechin equivalents per gram of dry weight, with calculations derived from a catechin calibration curve ($y = 0.0028x$, $R^2 = 0.988$).

Antioxidant activity assessment

The antioxidant activity of the plant extract and synthesized nanomaterials was evaluated using the DPPH radical scavenging assay [35–38], with ascorbic acid serving as the reference standard. Samples were serially diluted in methanol, and each dilution was combined with a 0.135 mM solution of DPPH. The mixtures were incubated in the dark for 30 min to allow the reaction to proceed. Following incubation, the absorbance was recorded at 517 nm using a spectrophotometer. The percentage of remaining DPPH radicals was calculated using the formula (Eq. 1):

$$\%\ \text{DPPH radical remaining} = ([\text{DPPH}]t / [\text{DPPH}]0) \times 100 \quad (1)$$

The correlation between the percentage of DPPH radical remaining and the sample concentration was analyzed by plotting the data on an exponential curve. From this, the IC_{50} value was calculated, representing the concentration needed to inhibit 50% of DPPH radicals. A lower IC_{50} value signifies stronger antioxidant activity.

Antibacterial activity assessment

Bacterial species

The antibacterial activity was evaluated against a panel of bacterial strains, including Gram-negative species: *Escherichia coli* (ATCC 25922), *Salmonella typhimurium* (ATCC 14028), and *Klebsiella pneumoniae* (ATCC 13883), as well as Gram-positive species: *Bacillus subtilis* (ATCC 6051), *Bacillus cereus* (ATCC 14579), and *Staphylococcus aureus* (ATCC 29213).

Agar well diffusion method

The agar well diffusion method was employed to assess the antibacterial activity of the nanomaterials. The microbial inoculum is evenly spread across the agar plate surface [39]. A sterile cork borer or tip creates an 8 mm diameter well in the agar. A 100 µL volume of the solution at the desired concentration is added to the well. The agar plates are incubated under optimal conditions for the test microorganism. The antibacterial agent diffuses through the agar medium, inhibiting the growth of the tested microbial strain. All nanocomposites and the plant extract's stock solutions were prepared fresh. Powders of *G. glabra* extract and the synthesized

nanocomposites were taken and dissolved in sterile distilled water in known concentrations: *G. glabra* extract (16.42 mg/mL), MgO/Fe_2O_3 NC (12.32 mg/mL), MgO/Fe_2O_3–chitosan NC (8.76 mg/mL), and MgO/Fe_2O_3–chitosan–curcumin NC (11.14 mg/mL). Standard antibiotic Azithromycin was applied as a positive control at a concentration of 2 mg/mL. All solutions were vortexed and sonicated for 10–15 min for complete dissolution and homogeneity. Preparations were used freshly in the agar well diffusion assay for the evaluation of antibacterial activity against selected Gram-positive and Gram-negative bacterial strains.

Anticancer activity assessment

Modifying cell cultures and treatment

Human cell lines A549 and WI-38 (ATCC, Manassas, VA, USA) were cultivated at 37 °C in a humidified 5% CO_2 atmosphere in DMEM (Dulbecco's Modified Eagle Medium, Cat# 11965092, Thermo Fisher Scientific, Waltham, MA, USA) supplemented with 10% FBS (Fetal Bovine Serum, Cat# 16000044, Thermo Fisher Scientific) and antibiotics (100 U/mL Penicillin, 100 µg/mL Streptomycin, Cat# 15140122, Thermo Fisher Scientific). Cells utilized in 40–50% of tests were subcultured at 80–90% confluency. The morphological examination was done at 24 and 48 h; however, the treatments were given for 48 h. Drug concentrations were calculated according to half-maximal inhibitory concentrations (IC_{50}/2) [40].

Cell survival assessment

The MTT test (Cat# M6494, Thermo Fisher Scientific) measured cell viability [41]. A549 and WI-38 cells were cultivated in 96-well plates (Cat# 3599, Corning, Corning, NY, USA) and exposed to different doses of chitosan (Cat# 448877, Sigma-Aldrich) and curcumin (Cat# C1386, Sigma-Aldrich, St. Louis, MO, USA) for 48 h. After adding the MTT reagent, formazan crystals were dissolved in DMSO (Dimethyl Sulfoxide, Cat# D8418, Sigma-Aldrich). Cell viability was estimated in comparison with untreated controls using a microplate reader (SpectraMax M5, Molecular Devices, San Jose, CA, USA) to detect absorbance at 570 nm. GraphPad Prism 9.5.3 (GraphPad Software, San Diego, CA, USA) was used to calculate IC_{50} values.

Determining the efficacy of drug combinations index (CI)

The combined effects of the drugs were assessed using the Chou-Talalay method with CompuSyn software. This analysis determined if the drugs worked better together (synergy), worse together (antagonism), or independently (additive). The dose reduction index (DRI_{50}) was calculated to measure how much the dosage of each drug could be lowered when combined without losing effectiveness [42].

ADME predictions

Computational techniques were used to evaluate the compound's absorption and dispersion characteristics. The SwissADME function in the BIOVIA Discovery Studio program was used to compute the lipophilicity (LogP) essential for comprehending the compound's absorption capacities. Additionally, SwissADME forecasted water solubility, which directly affected the compound's absorption in the gastrointestinal system and helped assess its solubility in watery conditions. SwissADME provided information on the compound's absorption efficiency after consumption by subjectively evaluating the potential for gastrointestinal (GI) absorption as high, moderate, or low. SwissADME was also utilized to estimate the compound's capacity to penetrate the brain by predicting blood–brain barrier (BBB) permeability. AdmetSAR was used to forecast metabolism and toxicity (admetSAR-2.0; http://lmmd.ecust.edu.cn/admetsar2), which revealed information on the compound's metabolic stability in the liver and possible genotoxicity, which indicates the possibility of generating genetic mutations [43].

Statistical analysis

All of the results are expressed as mean value ± standard deviation (SD), and all experiments were performed in triplicate to ensure reproducibility. Statistical analyses were conducted using GraphPad Prism version 9.5.3 (GraphPad Software, San Diego, CA, USA). Differences between multiple groups were evaluated using one-way analysis of variance (ANOVA) followed by Tukey's post hoc test or Student's t-test as appropriate. A p-value less than 0.05 ($p < 0.05$) was considered statistically significant. Dose–response curves were fitted using nonlinear regression to calculate IC_{50} values for antioxidant and cytotoxicity assays.

Results and discussion

Plausible mechanism of formation of NC

Mechanism of formation of MgO/Fe_2O_3 NC

The green synthesis of MgO/Fe_2O_3 NC involves a multifaceted collaboration of chemical and biological processes (Fig. 1). Magnesium sulfate and ferric sulfate dissolve in aqueous solution, releasing Mg^{2+} and Fe^{3+} ions. Simultaneously, bioactive polyphenols and flavonoids, such as Caffeic acid and liquiritigenin, are extracted from *G glabra* [44].

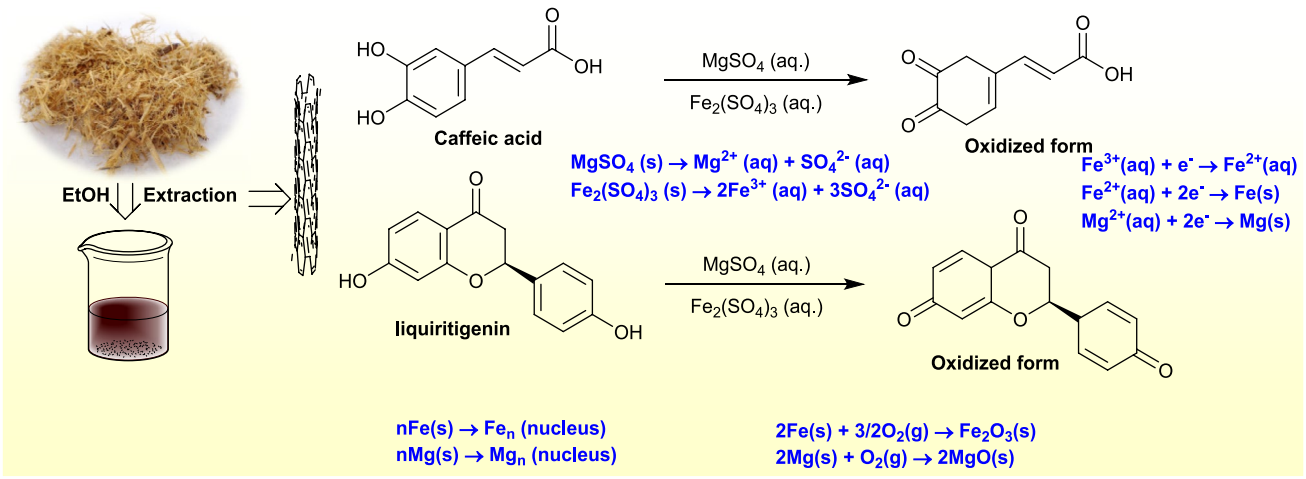

Fig. 1 The proposed mechanism for the formation of MgO/Fe_2O_3 NC. All chemical species and stages are labeled for clarity

These phytochemicals act as both reducing and capping agents. The reducing agents donate electrons to the metal ions, reducing them to their elemental forms (Fe^{2+}, Fe^0, and Mg^0) [45]. Subsequently, these reduced metal atoms aggregate and form nuclei, which serve as seeds for further growth [46]. The formed metal NPs are then oxidized by oxygen in the solution, forming MgO and Fe_2O_3 NPs [47]. The phytochemicals also act as capping agents, adsorbing onto the surface of the NPs, preventing further growth and agglomeration [48]. This stabilization process controls the size and shape of the NPs. The final product is a composite material comprising MgO and Fe_2O_3 NPs, whose properties are influenced by reactant concentrations, reaction temperature, and the specific phytochemicals in the extract.

Possible interactions between MgO/Fe_2O_3 NC and chitosan

The interaction between MgO/Fe_2O_3 NC and chitosan leads to NC with enhanced properties. Electrostatic interactions between NC's charged surface and chitosan's positively charged amino groups contribute to adsorption and composite formation [49]. Hydrogen bonding between hydroxyl groups in chitosan and oxygen atoms in the NPs further stabilizes the composite [50]. Additionally, coordination bonding between metal ions in NC and functional groups in chitosan strengthens the interaction [51]. Incorporating chitosan enhances the biocompatibility, dispersion, controlled drug release, and mechanical properties of MgO/Fe_2O_3 NC [52].

Plausible interactions between MgO/Fe_2O_3-CS NC and curcumin

The incorporation of curcumin into MgO/Fe_2O_3 NC–chitosan NC could form a synergistic effect, enhance their functions, and use [53]. Curcumin molecules physically adsorb on nanomaterial surfaces through van der Waals interactions and hydrophobic interactions, thereby stabilizing curcumin and inhibiting its degradation [54]. Also, the phenolic hydroxyl group of curcumin can form hydrogen bonds with chitosan functional groups and with metal ions via chelation or coordination bonding [55]. Additionally, curcumin molecules can be trapped within the pore space of nanomaterials, protecting them from degradation and enabling controlled release [56].

Characterization of nanomaterials

UV–visible spectroscopy analysis

UV–visible spectroscopy was employed to investigate the optical properties of the synthesized nanomaterials. The absorbance spectra of the *G. glabra* extract, MgO/Fe_2O_3, MgO/Fe_2O_3–chitosan, and MgO/Fe_2O_3–chitosan–curcumin NC were recorded, and the results are presented in Fig. 2a. The *G. glabra* extract exhibited a prominent absorption peak at 486 nm, attributed to bioactive compounds with chromophoric groups with conjugated π-electron systems [57]. This could be attributed to the presence of flavonoids, phenolic compounds, or other bioactive compounds in the *G. glabra* extract, in which the absorption likely arises from $\pi \rightarrow \pi^*$ transitions within these conjugated systems. The MgO/Fe_2O_3 NC showed a strong absorption band centered at 534 nm, indicating the nanomaterial's successful formation and electronic transitions within the nanostructure.

The red shift of the absorption peak to 534 nm compared to the extract suggests a change in the electronic structure of the nanomaterial [58]. This could be due to the interaction between the metal oxide NPs and the organic components of the extract. The red shift might be associated with forming

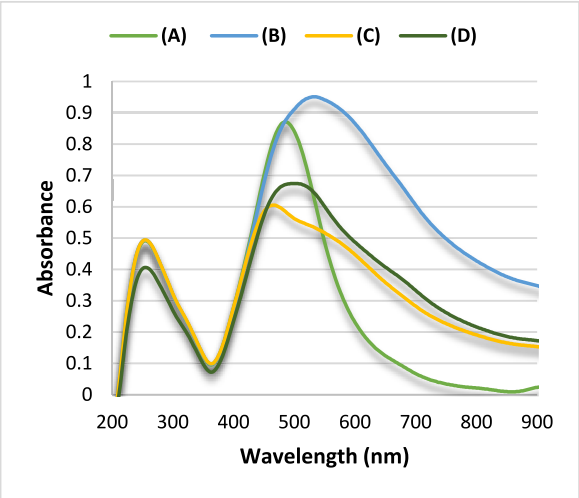

(a) The sample absorbance readings are recorded at different wavelengths.

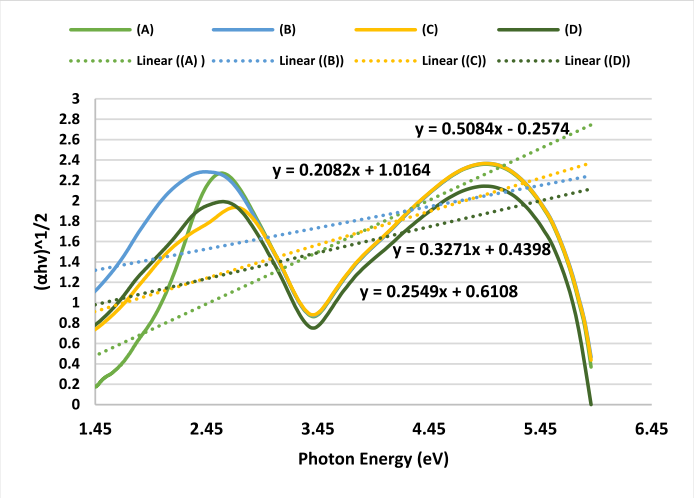

(b) Tauc plots of $(\alpha h\nu)^{1/2}$ versus photon energy (hν).

Fig. 2 UV–visible spectral data and Tauc plots of the *G. glabra* extract and synthesized nanomaterials. **A** *G. glabra* Extract; **B** MgO/Fe_2O_3 NC; **C** MgO/Fe_2O_3–chitosan NC; and **D** MgO/Fe_2O_3–chitosan–curcumin NC. Wavelength is measured in nm. Absorbance values are unitless

new electronic states or extending the conjugated π-electron system [59]. Upon incorporating chitosan, the absorption peak shifted to 466 nm, suggesting a change in the electronic structure of the nanomaterial. The blue shift of the absorption peak to 466 nm indicates a change in the electronic structure due to the interaction between chitosan and the metal oxide NPs, leading to alterations in the bandgap and optical properties [60]. The blue shift of the absorption peak compared to the MgO/Fe_2O_3 NC suggests a decrease in the energy gap between the highest occupied molecular orbital (HOMO) and the lowest unoccupied molecular orbital (LUMO) [61]. This could be attributed to the interaction between chitosan and the metal oxide NPs, leading to changes in the electronic structure. The red shift of the absorption peak to 498 nm of MgO/Fe_2O_3–chitosan–curcumin NC compared to the MgO/Fe_2O_3–chitosan NC can be attributed to the presence of curcumin, which has extensive conjugated π-electron systems. Curcumin can interact with the nanomaterial, leading to an extension of the conjugated system, which interacts with the nanomaterial and induces a bathochromic shift in the absorption spectrum [62].

The bandgap energy (Eg) for optical of as-prepared materials, obtained from Tauc plots (Fig. 2b), shows a declining trend through the samples: 1.65 eV for MgO/Fe_2O_3 NC, 1.56 eV for MgO/Fe_2O_3–chitosan, and 1.53 eV for MgO/Fe_2O_3–chitosan–curcumin NC, with the *G. glabra* extract having a bandgap of approximately 1.47 eV. This gradual reduction in bandgap energy is a result of alterations at a basic level in the π-conjugation's electronic structure and functionality with surface modification and functionalization. Introduction of chitosan and curcumin adds new conjugated systems and functional groups, which are in contact with the metal oxide matrix and introduce new tail states or localized states near the band edges. These effectively lower the bandgap to enable efficient charge transfer and better optoelectronic and photocatalytic behavior of the materials. The trend is also validated by UV–Vis absorbance spectra, where shifts in the spectrum also indicate the change of electronic transitions with higher organic content in addition to surface interactions within the nanocomposite material.

FTIR spectra of *G. glabra* extract-derived nanomaterials

The FTIR analysis was performed on the *G. glabra* extract and nanomaterials (Fig. 3), which verified the successful synthesis and incorporation of chitosan and curcumin into the nanomaterials. The *G. glabra* extract exhibited characteristic peaks at 3437 cm^{-1} (O–H stretch), 2919 and 2849 cm^{-1} (C-H stretch), 1632, 1606, 1576, and 1513 cm^{-1} (C = C stretch), and 1282, 1215, 1110, 1074, and 1045 cm^{-1} (C-O stretch), indicating the presence of alcohols, phenols, aromatic compounds, and other functional groups. The FTIR spectrum of $MgO\text{-}Fe_2O_3$ NC revealed characteristic absorption bands at 3428 cm^{-1} (O–H stretch), 2919 and 2849 cm^{-1} (C-H stretch), 1650 and 1607 cm^{-1} (C = C stretch), and lower frequency bands associated with metal–oxygen bond vibrations (M–O). O–H and C-H stretching vibrations are the signature of hydroxyl groups on the surface of NPs and residual organic material from the synthesis [63]. The C = C stretching vibrations inform us of the presence of aromatic

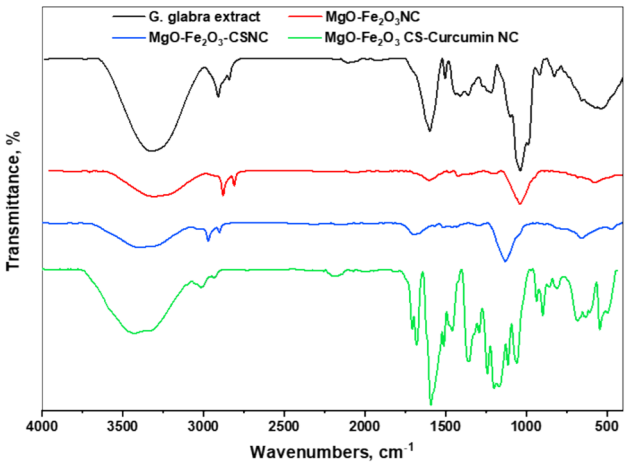

Fig. 3 The FTIR spectral analysis of *G. glabra* extract-based nanomaterials

compounds or unsaturated bonds, maybe because of the incorporation of the *G. glabra* extract. Metal–oxygen bond vibration verifies the formation of metal oxide NPs [64].

FTIR spectrum of MgO-Fe_2O_3-CS NC displayed characteristic absorption bands at 3453 and 3405 cm^{-1} (O–H stretch), 2918 and 2849 cm^{-1} (C-H stretch), 1649 and 1602 cm^{-1} (C = O and C = C stretch), and low frequency bands due to metal–oxygen bond vibrations and C-N stretching. The presence of O–H and C-H stretching vibrations is evidence of hydroxyl groups in chitosan [65]. Stretching vibrations of C = O and C = C confirm the presence of amide groups in chitosan and possibly leftover organic materials. Metal–oxygen bond metal stretching vibrations disclose the presence of metal oxide NPs, while C-N stretching vibrations are characteristic of chitosan [66]. FTIR spectrum of MgO–Fe_2O_3–Cs–curcumin NC exhibited the characteristic absorption bands at 3420 and 3350 cm^{-1} (O–H stretch), 2849 cm^{-1} (C-H stretch), 1622, 1598, 1586, and 1536 cm^{-1} (C = O and C = C stretch), and lower frequency bands corresponding to C-O stretching vibrations, C-H bending vibrations, and metal–oxygen bond vibrations. O–H and C-H stretching vibrations verified the presence of hydroxyl groups in curcumin. The C = O and C = C stretching vibrations are characteristic of conjugated carbonyl groups and aromatic rings in curcumin. The metal–oxygen bond vibrations confirm the presence of metal oxide NPs, while the other bands indicate the presence of various functional groups associated with curcumin and chitosan.

Energy-dispersive X-ray spectroscopy (EDX)

The EDX spectrum shown in Fig. 4 verifies the elemental composition of the prepared nanomaterials. In MgO/Fe_2O_3 NC, the principal elements identified were carbon (C) at 50.68 atomic%, oxygen (O) at 29.37 atomic%, magnesium (Mg) at 6.19 atomic%, and iron (Fe) at 13.76 atomic%, verifying the effective synthesis of the binary metal oxide composite. Upon addition of the chitosan to the MgO/Fe_2O_3 matrix, the elemental analysis was completely altered, with nitrogen (N) appearing at 25.87 at%, a clear indication of the chitosan, carbon reducing to 31.42 atomic%, and oxygen rising to 30.14 atomic%.

Further functionalization with curcumin equally increased the carbon (34.20 atomic%) and oxygen contents (33.49 atomic%), while nitrogen content slightly decreased to 21.83 atomic%. The magnesium signal remained at 3.96 atomic%. These findings verify effective sequential functionalization of the nanocomposite with chitosan and curcumin through changes in elemental distribution. Notably, our measured carbon content of the work well compared with the previous reports for other comparable nanomaterials [67, 68]. The EDX analysis confirms the successful synthesis of the target nanomaterials from *G. glabra* extract as a green reducing and capping agent, as specified by the detection of the anticipated elements and their relative percentages.

Zeta potential

Zeta potential measurements were conducted to assess the surface charge of the synthesized nanomaterials (Fig. 5). The MgO/Fe_2O_3 NC exhibited a zeta potential of −7.9 mV, suggesting a moderate negative surface charge (Fig. 5a). This moderate negative charge can contribute to the stability of the NPs in aqueous solutions, preventing aggregation. The introduction of chitosan into the MgO/Fe_2O_3 NC (Fig. 5b) reduced the zeta potential significantly to −0.4 mV. This proximity to a neutral surface charge may indicate reduced surface charge density or perhaps even shielding effects by the polymer chains of chitosan. The introduction of curcumin into the MgO/Fe_2O_3–chitosan NC (Fig. 5c) resulted in an extremely minor increase in the zeta potential to −7.3 mV. This is a sign that the incorporation of curcumin molecules may have affected the surface charge characteristics of the NPs. The observed values of zeta potential can be attributed to several factors, including the surface functional groups [69], the surface ionization level [70], and the interactions of the NPs with the environment [71]. The nanomaterials' negative surface charge has the potential to interact with positively charged molecules, such as cell membranes and proteins, which may have implications for their biological applications.

High-resolution transmission electron microscopy (HR-TEM)

HR-TEM was employed to analyze the morphology, particle size, and crystal structure of as-synthesized MgO/

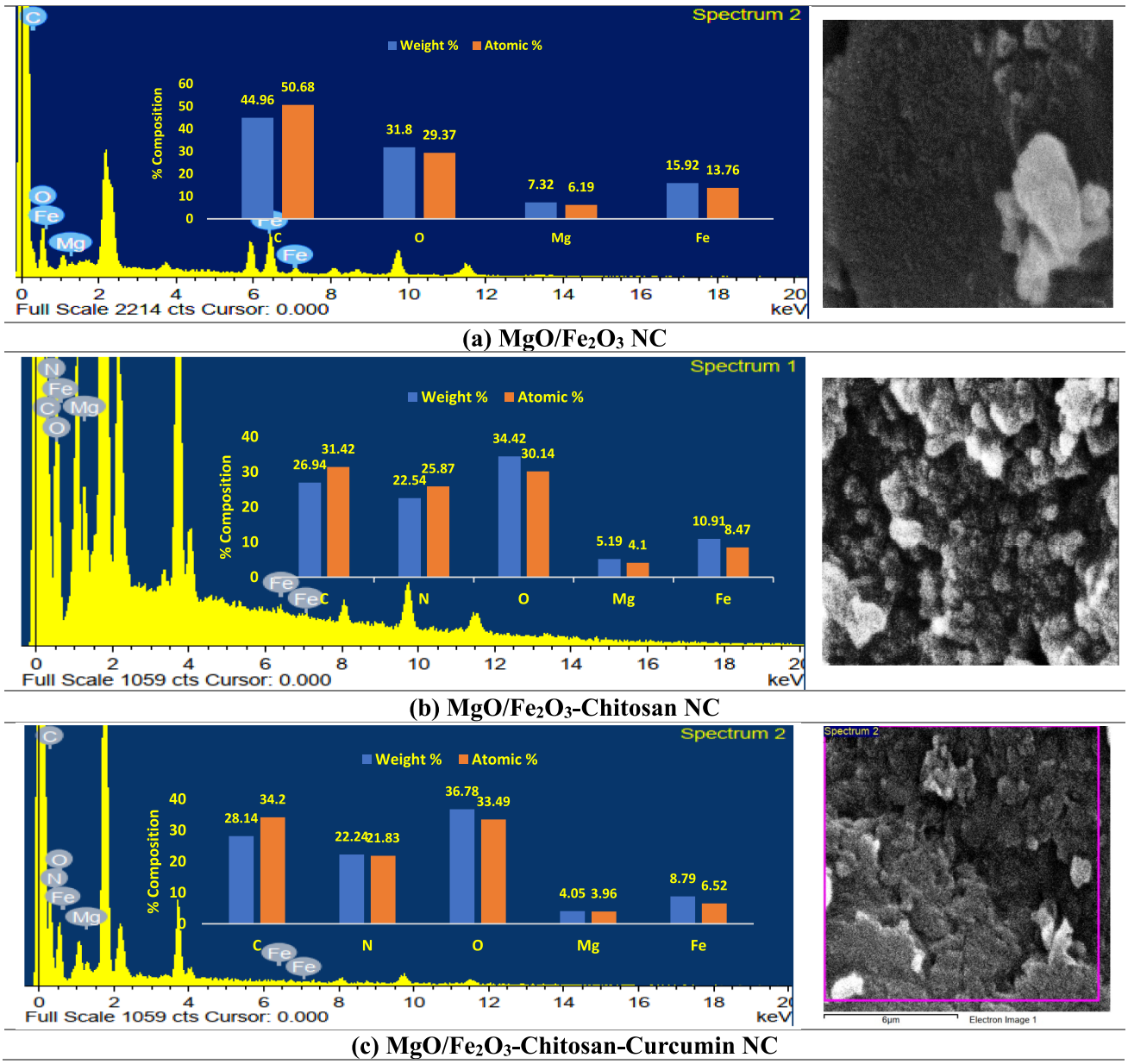

Fig. 4 EDX analysis of **a** MgO/Fe_2O_3 NC, **b** MgO/Fe_2O_3–chitosan NC, and **c** MgO/Fe_2O_3–chitosan–curcumin NC. *X-axis* Energy (keV), *Y-axis* Intensity (a.u.)

Fe_2O_3 NC (Fig. 6a). HR-TEM images revealed the formation of well-dispersed spherical NPs with an approximate average particle size of 20 nm. The size distribution of the NPs is small, indicating good uniformity of synthesis. The lattice fringes of the HR-TEM image suggest that the NPs are crystalline. The interplanar space between the lattice fringes can be measured to determine the crystallographic orientation and the crystal phase of the NPs. By comparing the computed interplanar spacing with known values for different crystal structures, the crystal phase of the NPs can be determined. HR-TEM of MgO/Fe_2O_3–chitosan NC (Fig. 6b) showed the development of agglomerated NPs with irregular shapes and dimensions. Chitosan in the composite material appears to have affected the morphology of the NPs, resulting in the development of aggregated structures. The NPs agglomerate, and this could be a result of chitosan, which is a binding agent among the NPs. The particle size distribution is relatively broad, ranging from a few nanometers to tens of nanometers. Crystallization might have been prevented by the presence of chitosan, resulting in amorphous or poorly crystalline domains in the NPs. Chitosan can modify the surface properties of the

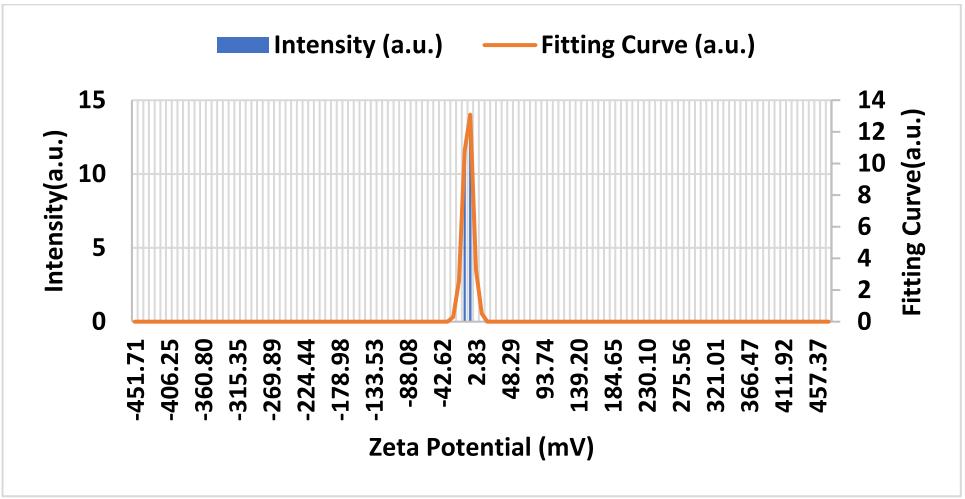

(a) MgO/Fe_2O_3 NC

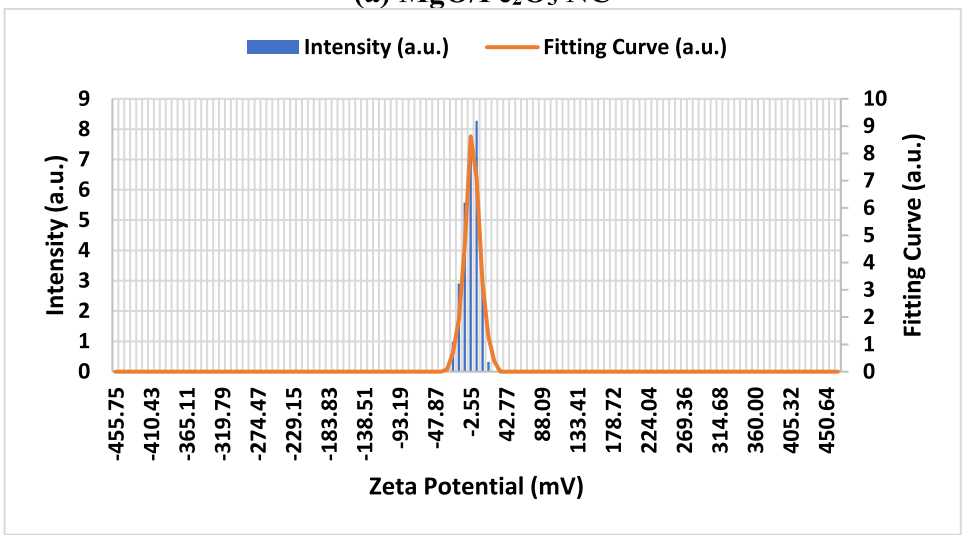

(b) MgO/Fe_2O_3-Chitosan NC

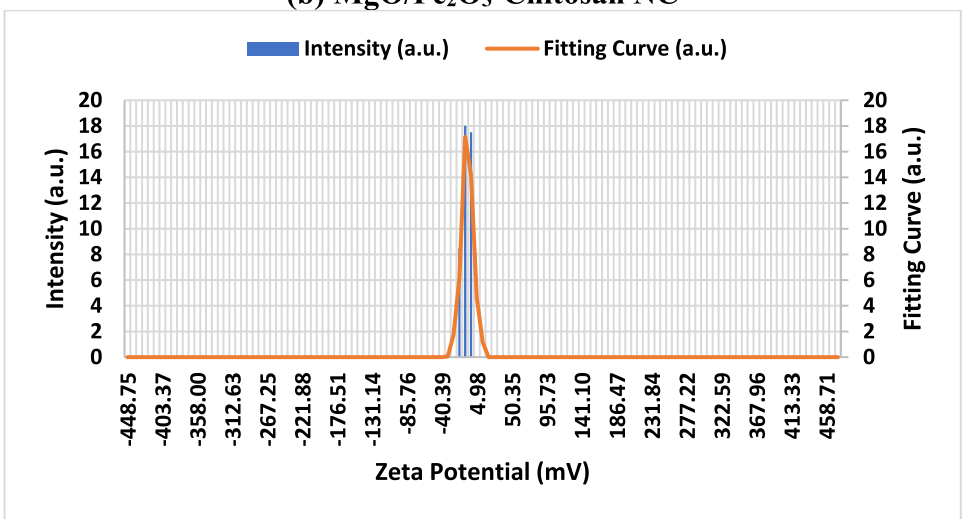

(c) MgO/Fe_2O_3-Chitosan-Curcumin NC

Fig. 5 Zeta potential of the synthesized nanomaterials. Units are in millivolts (mV)

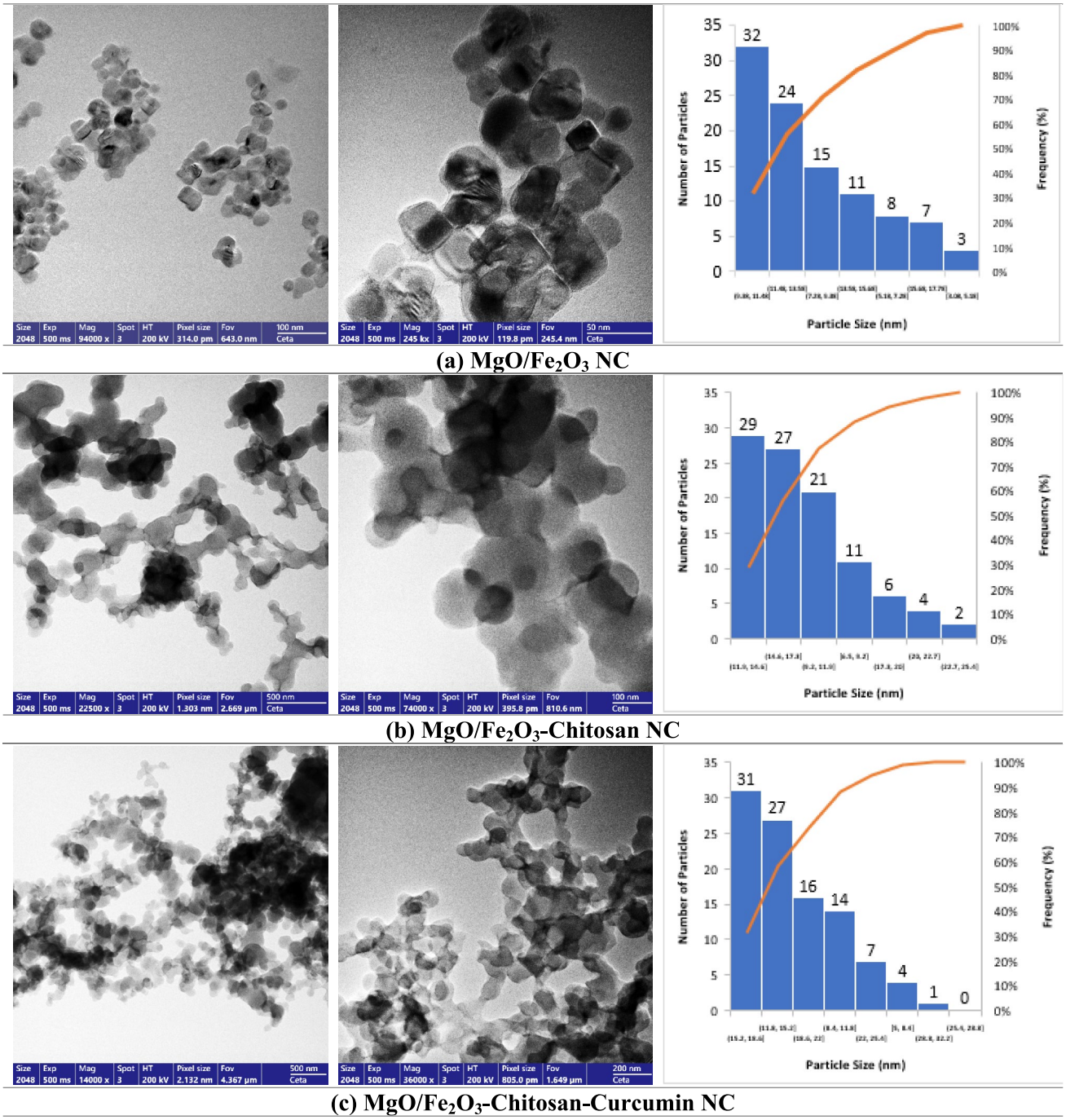

Fig. 6 HR-TEM micrographs and size distribution of the nanomaterials. Scale bars: 100 nm. Images were acquired at magnifications between 100,000 × and 300,000 ×

NPs and determine their interaction with other materials and solution dispersibility. Chitosan can also influence the growth and nucleation behaviors of the NPs, leading to modifications of their size and shape. Chitosan can also be used as a stabilizing agent, preventing agglomeration and promoting the colloidal stability of nanomaterials.

HR-TEM image of MgO/Fe_2O_3–chitosan–curcumin NC (Fig. 6c) shows the agglomerated NPs with irregular sizes and shapes. The availability of chitosan and curcumin in the composite material would have had some effects on the morphology of the NPs to create aggregated structures. The NPs are prone to agglomerate, which can be attributed to the

availability of organic constituents (chitosan and curcumin) and interparticle forces. The size distribution of the particles appears quite broad, with particles dispersed from a few nanometers up to tens of nanometers. The organic phase may have distorted the crystallization process, leading to amorphous or weakly crystalline domains within the NPs [72].

On the other hand, chitosan and curcumin can change the surface chemistry of the NPs, influencing their interactions with other materials and solution stability [73]. Chitosan and curcumin can also affect the growth and nucleation of the NPs, leading them to develop different sizes and shapes [31]. Chitosan can be employed as a stabilizer, which prevents agglomeration of the NPs and increases their colloidal stability [74]. Curcumin may also impart extra functions on the NPs, i.e., antioxidant features [75].

Scanning electron microscopy (SEM)

SEM was employed to investigate the morphology and surface features of the synthesized nanomaterials. The SEM images of MgO/Fe_2O_3 NC (Fig. 7a) revealed the formation of agglomerated NPs with irregular shapes. The particles appear to be porous and have a rough surface. The NPs are likely to form agglomerates, maybe because of strong interparticle forces. The distribution of the particle size is rather broad, and the particles are from a few nanometers to several tens of nanometers. The surface of the NPs is rough and porous, which may render their surface area greater and their catalytic activity or adsorption capacity stronger. SEM of MgO/Fe_2O_3–chitosan NC (Fig. 7b) showed the formation of agglomerated NPs with irregular shapes and sizes. The presence of chitosan in the composite material seems to influence the morphology of the NPs, and aggregated structures were formed. The NPs agglomerate, and this may be due to chitosan, which can also aggregate NPs. The size distribution of the particles is very wide, i.e., from a few nanometers to tens of nanometers. The NPs are porous in character, which can be favorable for increasing the surface area and thus their adsorption or catalytic efficiency. SEM micrographs of the MgO/Fe_2O_3–chitosan–curcumin NC prepared (Fig. 7c) revealed the formation of agglomerated NPs with irregular shape and size. The presence of chitosan and curcumin in the composite material seems to influence the morphology of the NPs, and agglomerated forms were achieved. The NPs agglomerate, perhaps due to the nature of organic components (chitosan and curcumin) and interparticle interactions. The particle size distribution appears to be very broad, ranging from a few nanometers to a few tens of nanometers.

Chitosan is a polycationic polymer that can electrostatically bind to the negatively charged surface of the metal oxide NPs [76]. This interaction can create a protective covering over the NPs, which can inhibit agglomeration and enhance their stability [77]. Furthermore, chitosan possesses hydroxyl and amino groups, which are capable of creating hydrogen bonds with the surface hydroxyl groups of metal oxide NPs [78]. Such hydrogen bonds have the potential to stabilize NPs further and affect their morphology [79]. Surface chitosan chains of the NPs can create a steric barrier that prevents particle aggregation [80]. Molecules of curcumin can be adsorbed onto the surface of the NP through van der Waals forces via physical adsorption [81].

Curcumin can also chemically bind to the surface functional groups of the NPs, such as hydroxyl or carboxyl groups [82]. Thus, the covalent or coordinate bonds can be established. Aromatic rings of curcumin can bind with surface aromatic groups of NPs through π-π stacking [83]. The integration of curcumin and chitosan into the NP system can synergistically interact with them. Chitosan can be used as a curcumin carrier to increase curcumin solubility and bioavailability [84]. Synergistic enhancement of NPs stability, biocompatibility, and therapeutic efficacy can be achieved by chitosan–curcumin mixture.

X-ray diffraction (XRD)

XRD analysis was performed to investigate the synthesized nanomaterials' crystalline phase and structural properties. The XRD patterns revealed the formation of crystalline phases corresponding to MgO and Fe_2O_3 (Fig. 8a). The XRD pattern of MgO/Fe_2O_3 NC exhibited characteristic peaks at 2θ angles of approximately 30.7°, 32.9°, 36.5°, 42.9°, 43.6°, 57.1°, and 62.7°, which can be indexed to the (220), (311), (222), (400), (331), (422), and (511) planes of cubic phase MgO (JCPDS card no. 45-0946). Additionally, peaks at 2θ angles of approximately 25.5°, 33.2°, 35.7°, 49.5°, 54.1°, and 57.6° were observed, which can be attributed to the (101), (110), (111), (211), (220), and (310) planes of hematite (α-Fe_2O_3) (JCPDS card no. 33-0664). These characteristic peaks establish the successful formation of a composite material with both the MgO and Fe_2O_3 phases present. The XRD pattern of MgO/Fe_2O_3–chitosan NC (Fig. 8b) revealed a distinct diffraction pattern from MgO/Fe_2O_3 NC. The peaks observed can be attributed to the combined effects of the crystalline phases of MgO, Fe_2O_3, and the amorphous nature of chitosan. The broad peak at $2\theta = 21.1°$ reflects the existence of an amorphous phase, possibly from the chitosan component. The upper 2θ peak maxima at 25.5°, 32.7°, and 40.2° may be attributed to the crystalline phases of MgO and Fe_2O_3, but due to the overlapping and broadening of peaks, their assignment to specific crystallographic planes cannot be ascertained with certainty [85]. Incorporation of chitosan into the nanomaterial structure may influence the crystallinity and size of crystallites of the inorganic component [86]. Its amorphous character may inhibit the crystalline phase growth to produce the broad diffraction peaks observed [87].

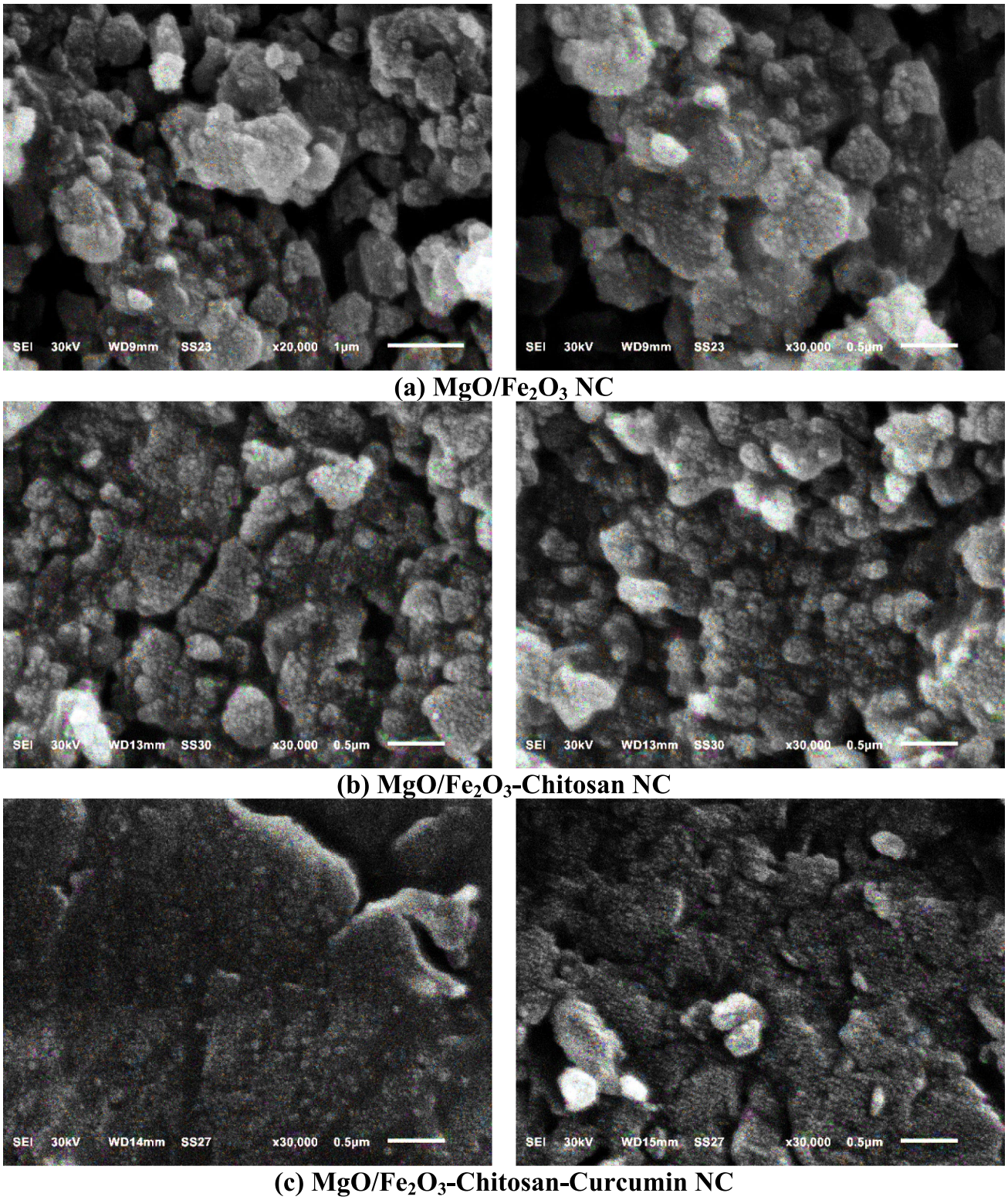

Fig. 7 SEM images of the nanomaterials. Scale bars: 200 nm. Images were captured at 20,000 and 30,000 × magnification

The XRD pattern of MgO/Fe_2O_3–chitosan–curcumin NC (Fig. 8c) reveals a similar trend to the MgO/Fe_2O_3–chitosan NC, with a significant contribution from the amorphous phase of chitosan. Nevertheless, the combination of curcumin might have impacted the crystallinity and crystallite size of the inorganic components [88]. The

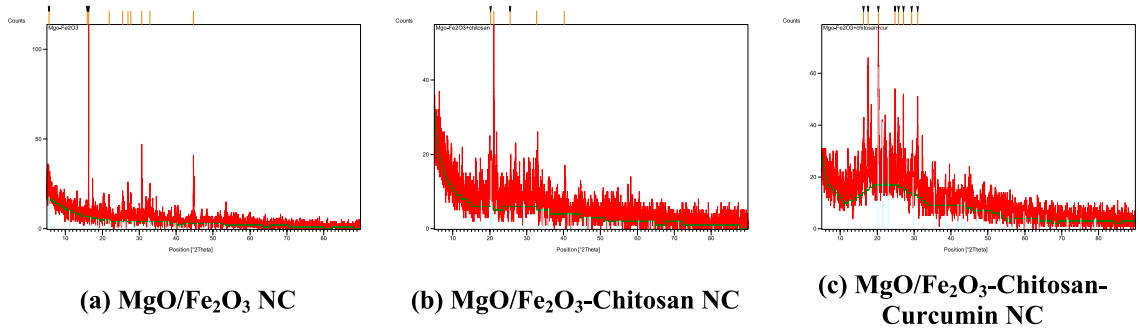

Fig. 8 XRD analysis of the synthesized nanomaterials. *X-axis* 2θ (degrees), *Y-axis* Intensity (a.u.)

broad peak centered around 2θ = 20.3° indicates the presence of an amorphous phase, predominantly attributed to the chitosan component. The peaks at higher 2θ angles, such as 25.8, 27.1, 29.4, and 30.9°, might correspond to the crystalline phases of MgO and Fe_2O_3, although the overlapping and broadening of these peaks make definitive peak assignments challenging. Curcumin, a polyphenolic compound, can potentially interact with the metal ions and influence the nucleation and growth of the inorganic phases [89]. The complex interrelation between the various constituents in the nanomaterial can bring about variation in crystallinity and size of the crystallites, as inferred from the XRD pattern.

Phytochemical analysis

The phytochemical analysis of the investigated samples, presented in Fig. 9, revealed significant variations in phenolic, flavonoid, and tannin content. The *G. glabra* extract exhibited the highest phenolic content (302.19 ± 1.88 mg gallic acid equivalent/g dry extract), indicating its potential as a rich source of antioxidants.

Like phenolic content, the *G. glabra* extract displayed the highest flavonoid content (134.1 ± 1.70 mg catechin equivalent/g dry extract). Incorporating *G. glabra* extract into the NC led to a substantial decrease in flavonoid content (Fig. 9). The *G. glabra* extract also exhibited the highest

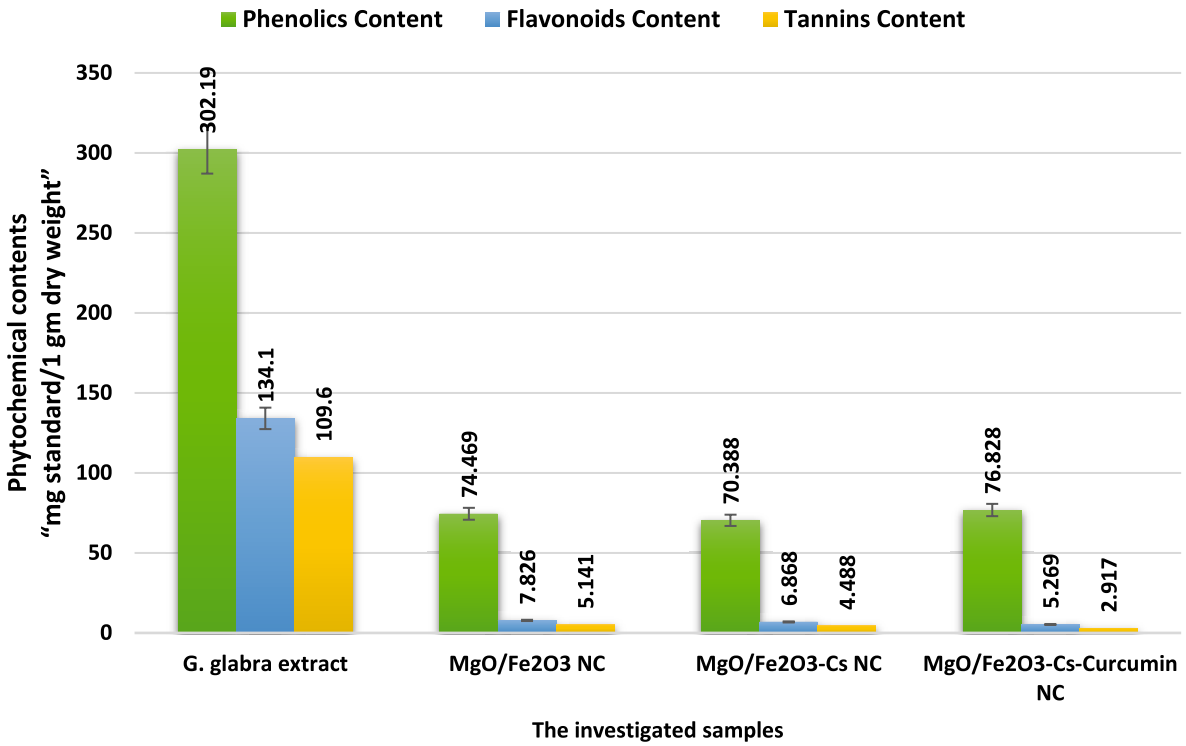

Fig. 9 A comparison of the phytochemical contents of the *G. glabra* extract and nanomaterials. Values are expressed as mg/g dry weight

tannin content (109.6 ± 1.76 mg tannic acid equivalent/g dry extract). Incorporating *G. glabra* extract into the NC resulted in a significant decrease in tannin content. Combining *G. glabra* extract in the biosynthesis of NC resulted in a considerable reduction in phytochemical contents. The decline in phytochemicals is attributed to the participation of phenolic components in the bioreduction process of metal ions during the formation of NC. The phytochemical compounds are then transformed into oxidized or dehydrogenated forms. The observed reduction in phytochemical content in the NC compared to the *G. glabra* extract suggests the successful biosynthesis process [90, 91]. The incorporation of curcumin into MgO/Fe_2O_3–Cs NC to form MgO/Fe_2O_3–Cs–curcumin NC led to an increase in the phenolic content owing to the nature of curcumin as a phenolic compound [92].

Antioxidant activity

Antioxidant activities of *G. glabra* extract and nanomaterials were tested through the DPPH radical scavenging assay (Fig. 10). The findings established the globally renowned excellent antioxidant activities of all samples through IC_{50} values, wherein the smaller IC_{50} value shows stronger antioxidant activity. In accordance with expectation, one of the reference antioxidants, ascorbic acid, showed maximum activity with an IC_{50} value of 0.0220 mg/mL. The *G. glabra* extract had excellent antioxidant capacity with an IC_{50} value of 0.0617 mg/mL. Interestingly, combining the *G. glabra* extract with the NC did not result in any substantial loss of antioxidant capacity compared with the pure extract. Of NCs, MgO/Fe_2O_3–Cs–curcumin NC had the strongest antioxidant capacity (IC_{50} = 0.0977 mg/mL), followed by MgO/Fe_2O_3-Cs NC (IC_{50} = 0.1135 mg/mL) and MgO/ Fe_2O_3 NC (IC_{50} = 0.1401 mg/mL).

The antioxidant activity of the samples was assessed using the DPPH radical scavenging assay. As shown in Fig. 11, the *G. glabra* extract exhibited significant antioxidant activity, with 82.6 ± 1.55% scavenging activity at a concentration of 0.128 mg/mL. The MgO/Fe_2O_3 NC with and without chitosan also have strong antioxidant activity, 1.28%–63.91% scavenging activities. Notably, the MgO/Fe_2O_3–Cs–curcumin NC possessed the greatest antioxidant activity of the tested samples with a 92.01 ± 1.15% scavenging capacity at a concentration of 0.288 mg/mL. Enhanced activity is due to the synergy of natural antioxidant curcumin and the nanomaterial advantages of high surface area and controlled release. Ascorbic acid, a standard antioxidant, was administered as a positive control and exhibited strong antioxidant activity with 84.73 ± 1.73% scavenging activity at the concentration of 0.06 mg/mL.

The enhanced antioxidant capacity of the curcumin-loaded NC is a result of the synergistic effect of curcumin, a unique structural nature as it is a phenol compound, and the characteristics of the nanomaterial, such as higher surface area and controlled release [92, 93]. The results are consistent with the results of phytochemical content. The enhanced antioxidant activity of MgO/Fe_2O_3-Cs NC may be attributable to the polyhydroxy group structure of chitosan, which may participate in the DPPH free radical scavenging [94]. The results show that the NC prepared, particularly the curcumin-encapsulated NC, possesses significant antioxidant activity and can have promising medicinal, food, and cosmetic applications.

DPPH is a stable free radical that has a violet color and contains one unpaired electron. On reaction with the

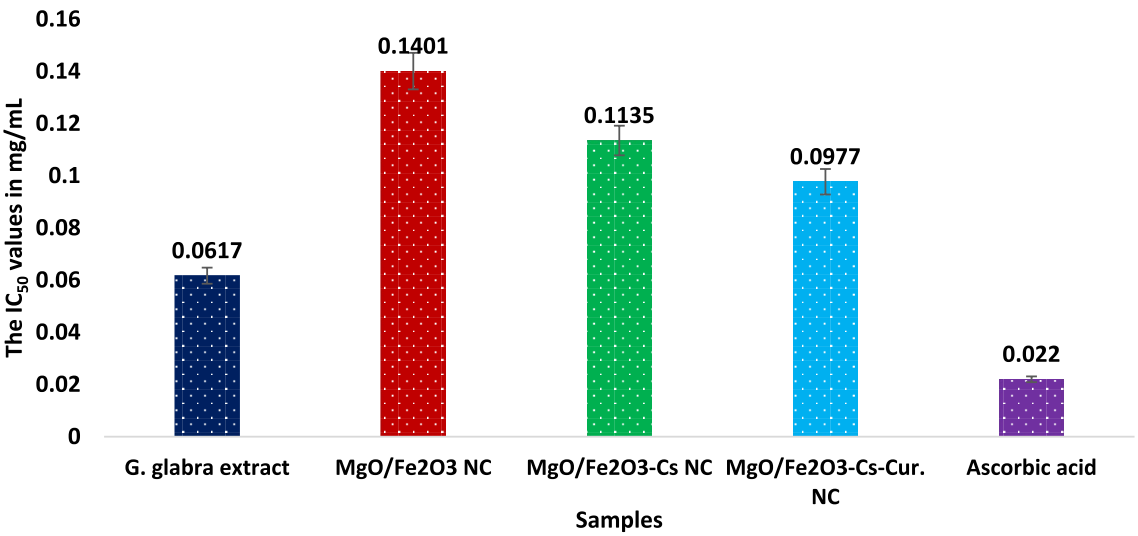

Fig. 10 Comparison of the antioxidant results expressed as IC_{50} in mg/mL of the investigated samples relative to the antioxidant standard

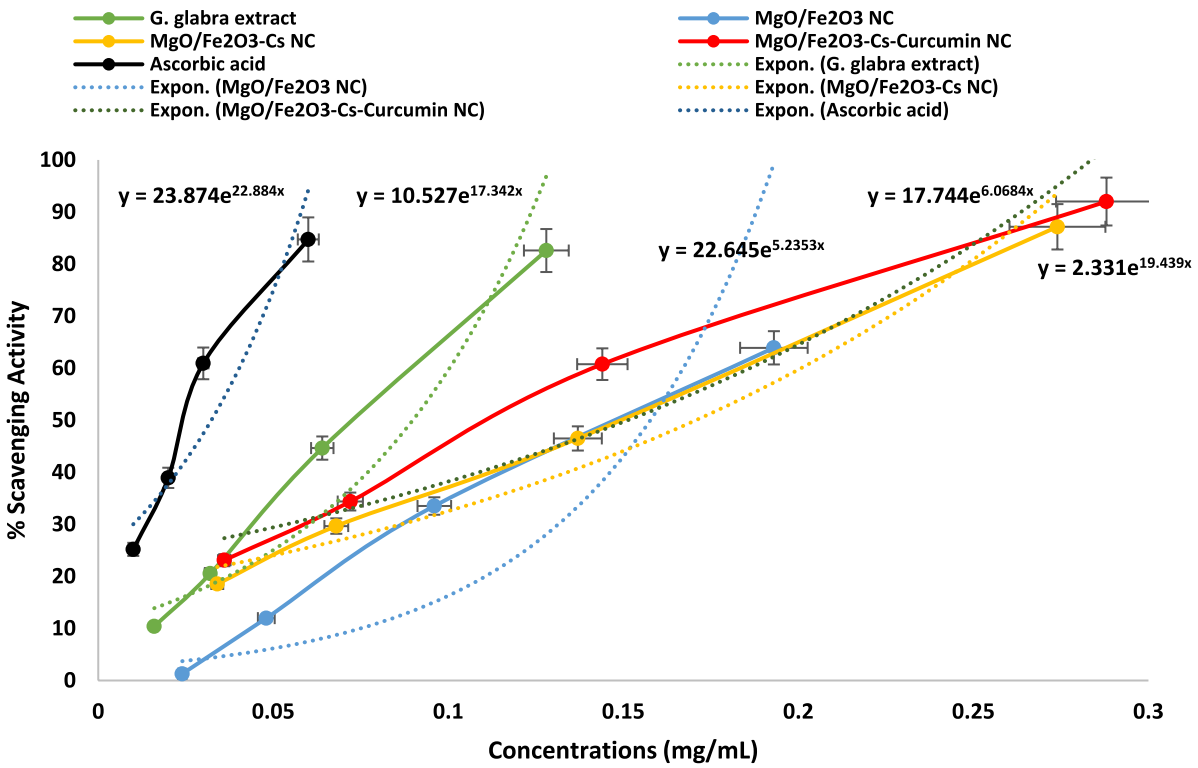

Fig. 11 The relationship between sample concentration (mg/mL) and % scavenging activity

antioxidant compound, the hydrogen atom is donated by the compound to the radical, which gets neutralized. Neutralization causes the color to change to yellow from deep purple. For the *G. glabra* extract, many phytochemical compounds like phenolics, flavonoids, and tannins are endowed with hydrogen donor activity [95]. These compounds donate a hydrogen atom easily to the DPPH radical and consequently reduce it to exhibit strong antioxidant activity.

Similarly, MgO/Fe_2O_3 NC and their derivatives can also interact with DPPH radicals. The chitosan and curcumin incorporated metal oxide NPs can expose additional sites for hydrogen atom transfer or electron donation [73]. The high surface area of NPs can promote increased interaction with DPPH radicals, enhancing antioxidant activity [96]. Curcumin, a bioactive molecule, can also contribute to the antioxidant character of the NC [92]. It may interact directly with DPPH radicals or indirectly through the neutralization of other free radicals. In general, the antioxidant activity of the *G. glabra* extract and the NC is influenced by various factors such as the incorporation of phenolic compounds, surface area, nanomaterials' physicochemical properties, and synergistic interactions among the different components [97].

Antibacterial activity

The antibacterial activity of MgO/Fe_2O_3-based NC was evaluated against Gram-negative and Gram-positive bacterial strains, with azithromycin as the positive control. The Gram-negative bacteria (*E. coli*, *S. typhimurium*, and *K. pneumoniae*) showed no inhibition zones when treated with MgO/Fe_2O_3-based NC, representing a lack of activity against these species. In contrast, azithromycin confirmed remarkable activity toward all Gram-negative strains, with inhibition zones ranging from 21.5 mm for *S. typhimurium* to 30.5 mm for *E. coli*. For Gram-positive bacteria, the findings are more favorable. *B. subtilis* displayed an inhibition zone of 10.5 ± 0.50 mm when treated with MgO/Fe_2O_3 NC, but no activity was perceived with MgO/Fe_2O_3-Cs NC or MgO/Fe_2O_3–Cs–curcumin NC. Likewise, *B. cereus* displayed inhibition zones of 11.5 ± 0.40, 10.5 ± 0.60, and 10.5 ± 0.60 mm for MgO/Fe_2O_3 NC, MgO/Fe_2O_3-Cs NC, and MgO/Fe_2O_3–Cs–curcumin NC, respectively. These findings recommend analogous activity through the tested NC against this strain. Remarkably, *S. aureus* displayed the highest sensitivity among the Gram-positive strains, with inhibition zones of 13.5 ± 0.60, 11.5 ± 0.70, and 11.5 ± 0.70 mm for MgO/Fe_2O_3 NC, MgO/Fe_2O_3-Cs NC, and MgO/

Fe_2O_3–Cs–curcumin NC, respectively. Azithromycin outperformed the NC against all Gram-positive strains, generating inhibition zones of 21.0 ± 1.3, 13.5 ± 1.7, and 19.5 ± 2.0 mm for *B. subtilis, B. cereus*, and *S. aureus*, respectively. In all, the findings confirm that while the NC exhibited decreased or no activity toward Gram-negative bacteria, they were active at a moderate level against certain Gram-positive bacteria, with the MgO/Fe_2O_3 NC being the most effective of the NC (Table 1 and Fig. 12). These findings suggest that chitosan and curcumin incorporation could have suppressed the antibacterial properties of the nanomaterial, possibly due to reduced surface area, altered surface charge, or interference with the release of active species.

Fine particle size of MgO/Fe_2O_3 NC can also improve antibacterial activity by having more surface area contact with bacterial cells [98]. NPs with smaller sizes have more surface area, leading to more contact with bacterial cells and more antibacterial action. In some applications, blending

Table 1 Antibacterial effects of NC on pathogenic bacterial strains

Bacterial species	MgO/Fe_2O_3 NC	MgO/Fe_2O_3–Cs NC	MgO/Fe_2O_3–Cs–curcumin NC	Azithromycin
Gram-negative species				
E. coli	− ve	−ve	−ve	30.5 ± 0.80
S. typhimurium	−ve	−ve	−ve	21.5 ± 2.00
K. pneumoniae	−ve	−ve	−ve	23.5 ± 1.50
Gram-positive species				
B. subtilis	10.5 ± 0.50	−ve	−ve	21.0 ± 1.30
B. cereus	11.5 ± 0.40	10.5 ± 0.60	10.5 ± 0.60	13.5 ± 1.70
S. aureus	13.5 ± 0.60	11.5 ± 0.70	11.5 ± 0.70	19.5 ± 2.00

Antibacterial activity of MgO/Fe_2O_3-based NC and azithromycin against Gram-negative and Gram-positive bacterial strains. Results are expressed as inhibition zones (mm) ± standard deviation. "−ve" indicates no inhibition zone observed

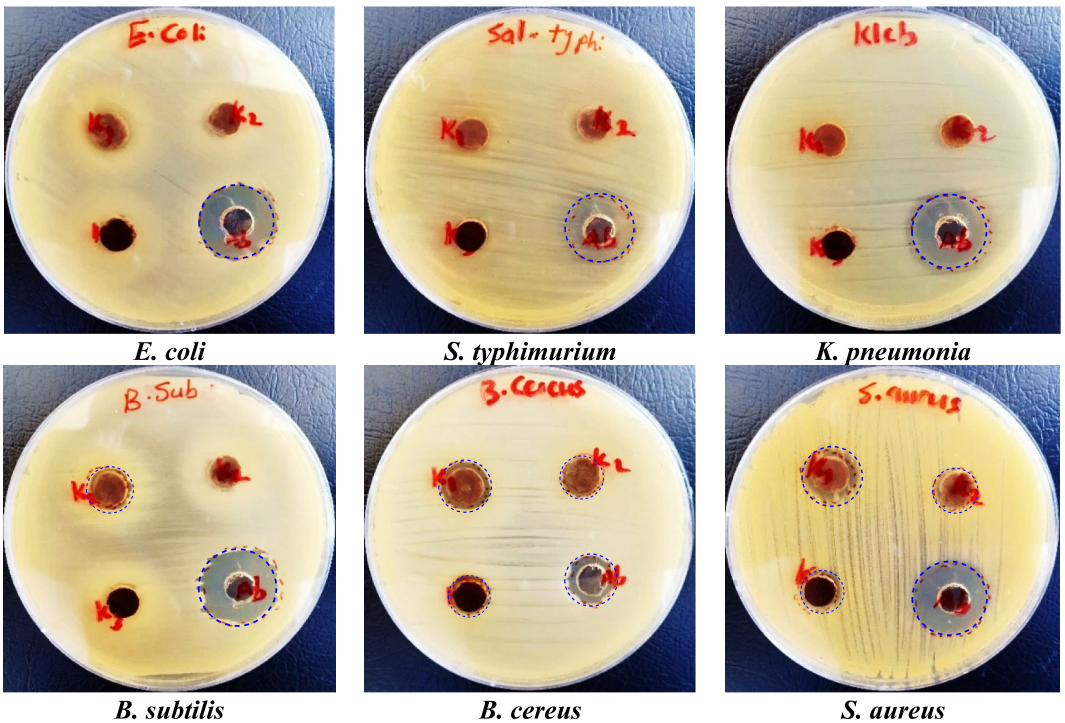

Fig. 12 Representative images of Petri dishes illustrating the antibacterial activity of the nanocomposites against various pathogenic bacterial strains. (K1) refers to MgO/Fe_2O_3 NC, (K2) corresponds to MgO/Fe_2O_3–chitosan (Cs) NC, (K3) denotes MgO/Fe_2O_3–Cs–curcumin NC, and (Ab) represents the standard antibiotic Azithromycin (2 mg/mL). The tested concentrations were as follows: *G. glabra* extract (16.42 mg/mL), MgO/Fe_2O_3 NC (12.32 mg/mL), MgO/Fe_2O_3-Cs NC (8.76 mg/mL), and MgO/Fe_2O_3–Cs–curcumin NC (11.14 mg/mL). Zone of inhibition diameters are shown in mm

materials can create synergistic effects, wherein the resulting action is more than the sum of individual actions [99]. While chitosan and curcumin are typically used to improve biocompatibility and drug delivery, they can also interfere with the antibacterial properties of the NPs [100]. The charge on the nanomaterials may also dictate how they will interact with the cell membranes of bacteria. Chitosan and curcumin can interfere with the direct interaction of NPs with bacterial cells and reduce their effectiveness [101].

Additionally, the nanomaterials are capable of generating reactive oxygen species (ROS), which may kill bacterial cells [102]. The nanocomposites may disrupt bacterial membrane integrity, leading to leakage of intracellular contents and oxidative stress due to ROS overproduction. However, despite being antibacterial themselves, chitosan and curcumin may interfere with the nanomaterial's antibacterial function by sticking to its surface or inhibiting the release of active species [103]. Antibacterial activity of nanomaterials can be regulated by various parameters, including particle size, form, charge, and mechanism of action type [104]. Experimental verification is thus a must to check the antibacterial activity of these materials.

The loss of antibacterial activity for functionalized chitosan and curcumin can be understood as a result of partial protection of reactive surface sites available for microbial interaction and ion release. The phytochemical and biopolymer layers would provide a steric barrier by reducing exposure of MgO/Fe_2O_3 nanoparticle surfaces to bacterial membranes. Furthermore, these coatings may retard diffusion of toxic metal ions and the generation of ROS, thus limiting immediate bactericidal activity. Even though this can reduce short-term antibacterial activity, it can simultaneously enhance targeted delivery and biocompatibility, both of which are most important for therapy, like cancer therapy.

Anticancer activity

Cytotoxicity, selectivity, and drug interaction studies of Mg-Fe NC

In this study, our primary aim was to evaluate the cytotoxicity profile and biocompatibility of the synthesized MgO/Fe_2O_3–chitosan–curcumin NC, rather than to benchmark its potency against standard chemotherapeutics such as doxorubicin. A key aspect of our assessment was the comparison of IC_{50} values between cancerous A549 cells and normal WI-38 fibroblasts. This selectivity analysis allowed us to determine the therapeutic index and safety margin of the NC. While doxorubicin is known for its potent anticancer effects, it also exhibits significant toxicity in normal cells. In contrast, cell viability assays revealed a dose-dependent response to all tested compounds in WI-38 cells, with IC_{50} values of 132.9 µg for curcumin, 109.5 µg for chitosan, 171.9 µg for chitosan–curcumin, and 220.9 µg for Mg-Fe NC-doped chitosan–curcumin. Combining chitosan and curcumin showed a lower cytotoxic effect than individual components, and the Mg-Fe NC-doped chitosan–curcumin formulation displayed the lowest cytotoxicity (Fig. 13). This indicates that the combination of curcumin and chitosan–curcumin was more effective than either compound alone, and adding Mg-Fe NC further reduced its toxicity. This suggests that the chitosan–curcumin combination and Mg-Fe NC incorporated into the chitosan–curcumin formulation could inhibit cell proliferation and cell death.

Furthermore, this favorable selectivity index highlights the biocompatibility of the NC in vitro. However, we acknowledge that comprehensive safety profiling should also include hemocompatibility, genotoxicity, and in vivo toxicity studies. Although these assays were beyond the scope of the current work, they are essential next steps in advancing this nanoformulation toward clinical application.

Further analysis of cell inhibition in A549 cells corroborated these findings. The compounds displayed varying degrees of cytotoxicity, with the Mg-Fe NC-doped chitosan–curcumin formulation again showing the most significant inhibitory effect, with an IC_{50} of 10 µg (Fig. 14). Combining treatments led to significantly lower cell survival compared to using either drug alone. Furthermore, the concentrations needed to reduce cell viability by 50% (DRI_{50}) were 11.24 for curcumin and 33.56 for chitosan (Table 2).

Morphological changes, including cell shrinkage, rounding, and detachment, were particularly evident in cells treated with chitosan–curcumin and Mg-Fe NC doped with chitosan–curcumin, especially after 48 h (Fig. 14). These findings confirm the enhanced cytotoxic potential of the chitosan–curcumin combination, which is further amplified by the inclusion of Mg-Fe NPs. These findings suggest a synergistic interaction between chitosan, curcumin, and Mg-Fe NC, enhancing their cytotoxic potential against cancer cells. Further research is warranted to explore these formulations' underlying mechanisms and therapeutic applications. This accords with the latest research highlighting the potential of multi-component nanotherapeutics to target multiple cancer pathways simultaneously, maximizing efficacy at lower side effects [105].

The ADME predictions

Computer simulations suggest that combining curcumin with chitosan and adding Mg-Fe NC significantly improves the delivery and effectiveness of curcumin against lung cancer cells. Curcumin alone cannot reach and kill cancer cells due to its poor water solubility and difficulty entering cells. However, when combined with chitosan, these issues are significantly reduced, and curcumin is better able to stay active in the body. Adding Mg-Fe NC further enhances the

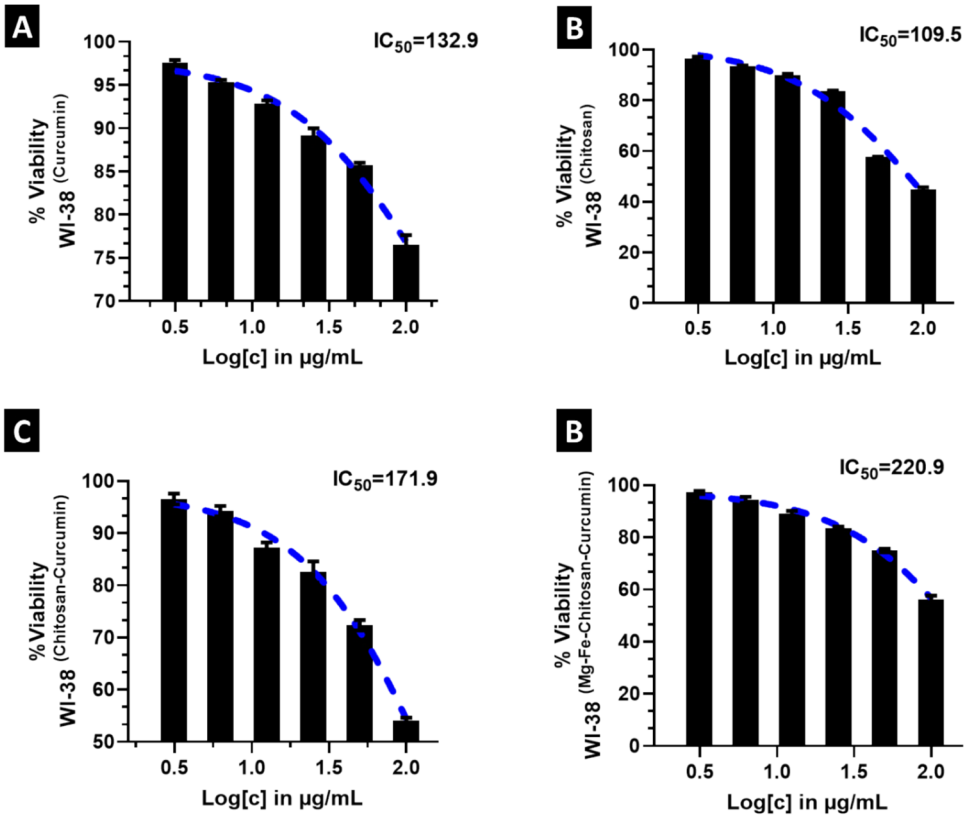

Fig. 13 Growth inhibition curves in WI-38 cells treated with **A** curcumin, **B** chitosan, **C** chitosan–curcumin, **D** MgO/Fe_2O_3 NC-doped chitosan–curcumin. The results were revealed as % of normal cell viability and averaged with standard deviation. The whole experiment was repeated at least three times. Error bars represent standard deviation. Each experiment was repeated in triplicate

drug's ability to reach and remain in lung cancer cells, leading to more substantial cancer-killing effects. These findings are consistent with reports that engineered nanomaterials, such as chitosan/cerium oxide hybrid and mesoporous silica vehicles, enhance bioavailability and therapeutic efficacy of insoluble drugs such as curcumin [106, 107]. While initial predictions indicate low toxicity and limited brain penetration, more research is needed to fully understand the safety and effectiveness of these formulations for long-term use (Table 3). Combining curcumin, chitosan, and metal NPs is the most promising approach for treating lung cancer among the tested options.

The evaluation of curcumin, chitosan, chitosan–curcumin, and Mg-Fe NC-doped chitosan-curcumin on A549 and WI-38 cell lines revealed significant cytotoxic effects, consistent with findings in other studies that have explored the potential of these compounds as anticancer agents. The dose-dependent decrease in cell viability observed across all tested formulations aligns with previous research demonstrating the anticancer properties of curcumin and chitosan [108, 109]. The Mg-Fe NC-doped chitosan–curcumin formulation exhibited the lowest IC_{50}, highlighting its superior cytotoxic activity. This finding corroborates the work of Lôbo et al. [110] and Li et al. [111], who reported that NPs-enhanced formulations can significantly improve anticancer agents' bioavailability and therapeutic efficacy. Additionally, this is consistent with prior work on nanoparticle-mediated drug delivery for overcoming chemoresistance in solid tumors such as colorectal and breast cancer [112, 113].

The morphological analysis provided further evidence supporting these results, with treated cells showing significant apoptotic changes such as shrinkage, rounding, and detachment, particularly after 48 h of treatment. These observations align with studies by Aggarwal [114] and Noor [115], which have documented similar apoptotic effects following treatment with Curcumin-based formulations. The enhanced cytotoxicity observed in the chitosan–curcumin and Mg-Fe NC-doped chitosan–curcumin formulations suggests a synergistic effect, consistent with the findings of Nayak [116] and Bai et al. [117], who highlighted the potential of NPs-mediated delivery systems to enhance the efficacy of combined anticancer therapies.

The selective cytotoxicity observed in cancer cells compared to normal cells, indicated by higher IC_{50} values in WI-38 cells, suggests a potential therapeutic window. The work of Mahjoubin-Tehran et al. supports this, and Shi et al. [119], who noted the importance of targeting cancer cells while minimizing damage to normal tissues. However, further research is necessary to fully establish the safety profile of these formulations, optimize their delivery, and elucidate the precise mechanisms driving their enhanced anticancer effects. Collectively, the findings from this study align with existing literature, indicating that the combination of chitosan and curcumin, particularly when enhanced with

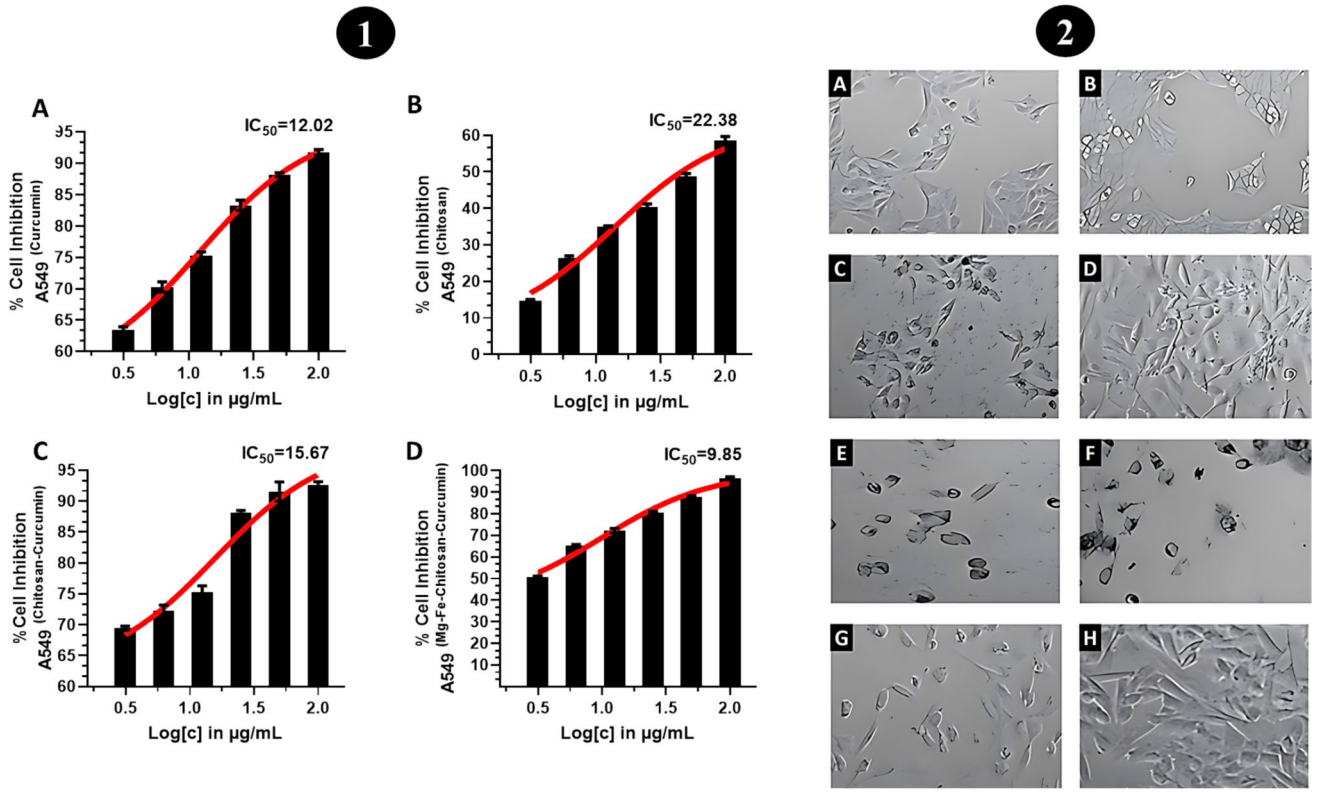

Fig. 14 Effect of (1A) Curcumin, (1B) Chitosan, (1C) Chitosan–curcumin, (1D) Mg-Fe NC-doped chitosan–curcumin on cell inhibition of A549. (2-A-D) Representative photographs displaying morphological changes in WI-38 cells exposed to $IC_{50}/2$ concentration of (2-A) Curcumin, (2-B) Chitosan, (2-C) Chitosan–curcumin, (2-D) Mg-Fe NC-doped chitosan–curcumin treatment for 24 and 48 h. (2E-H) Representative photographs showing morphological changes in A549 cells exposed to $IC_{50}/2$ concentration of (2-E) Curcumin, (2-F) Chitosan, (2-G) Chitosan–curcumin, (2-H) Mg-Fe NC-doped chitosan–curcumin treatment for 24 and 48 h. These features, such as shrinkage, rounding, and detachment, reflect cytotoxic effects aligned with IC_{50} values reported in Fig. 14. These changes indicate reduced viability and active inhibition of cancer cells. Scale bar = 50 µm

Table 2 Quantifying the synergistic or antagonistic interactions between curcumin and chitosan in A549 lung cancer cells

Cell line	Dose	DRI_{50}	CI_{50}	Interpretation
A549	Curcumin	11.24 µg/mL	4.21	Strong synergism
	Chitosan	33.56 µg/mL		

CI_{50} Combination index for the 50% effect

Mg-Fe NC, holds promise as a potent and targeted anticancer therapy.

Mechanistic insights into cytotoxicity

Although this study primarily focused on cytotoxic outcomes, the observed inhibition of A549 lung cancer cell proliferation by the MgO/Fe_2O_3–chitosan–curcumin NC is likely mediated by several well-documented cellular mechanisms. Curcumin is known to induce apoptosis via mitochondrial (intrinsic) pathways, including generation of ROS, depolarization of mitochondrial membrane potential, and activation of caspase enzymes such as caspase-3 and caspase-9 [120, 121]. Metal oxide nanoparticles, including MgO and Fe_2O_3, can further contribute to oxidative stress by promoting ROS accumulation, which may lead to lipid peroxidation, DNA damage, and activation of cell death pathways [122, 123]. Chitosan, in addition to enhancing cellular uptake, may facilitate the sustained intracellular delivery of active components [124]. Morphological observations of treated cells—such as shrinkage, rounding, and detachment—are consistent with apoptosis [114].

While this study primarily focused on the antioxidant, antibacterial, and anticancer activities of the MgO/Fe_2O_3–chitosan–curcumin NC, additional therapeutic effects warrant further investigation. However, this study presents promising results on the green synthesis and therapeutic potential of MgO/Fe_2O_3–chitosan–curcumin NC; several limitations should be acknowledged. First, the biological assessments were primarily conducted in vitro, limiting the direct extrapolation of findings to in vivo or clinical settings. Second, the mechanisms underlying the observed synergistic effects require further molecular and biochemical investigations to

Table 3 ADME prediction of Mg-FeNPs doped chitosan–curcumin on A549 lung cancer cells

Property	In Silico prediction (tool)	In vitro results (assay)	Notes
Absorption			
Lipophilicity (LogP)	Mg-FeNPs: 3.29 (SwissADME)	–	Moderate lipophilicity may enhance cellular uptake but is limited by solubility
Water solubility	Mg-FeNPs: 11 µg/mL (SwissADME)	–	Poor solubility in water limits absorption, but it is improved with chitosan and NPs
Cellular uptake	High (SwissADME)	Enhanced in A549 cells (MTT assay)	Enhanced uptake in A549 cells when combined with chitosan and Mg-FeNPs, suggesting better absorption
Distribution			
Blood–brain barrier (BBB)	Low (SwissADME)	–	Low BBB permeability; focus on non-neuro applications
Tissue distribution	–	Preferentially in A549 cells	Enhanced distribution in A549 cells due to NPs targeting
Metabolism			
Metabolic stability	Mg-FeNPs: moderate (AdmetSAR)	60% metabolized in A549 cells (HepG2 cells)	The metabolism rate improved with chitosan and further stabilized with Mg-FeNPs
Major metabolites	–	Curcumin-OH	Metabolites need further study for potential cytotoxicity or therapeutic activity
Excretion			
Excretion pathways	Biliary excretion (SwissADME)	Slow release in A549 cells	Slow excretion is likely due to the NP formulation, ensuring prolonged therapeutic effect
Toxicity			
Cytotoxicity	Strong (AdmetSAR)	$IC_{50} = 9.85$ µg (A549 cells)	Enhanced cytotoxicity in A549 cells with Mg-FeNPs doped chitosan–curcumin, the lowest IC_{50}
Genotoxicity	Low (AdmetSAR)	–	Low genotoxic potential is predicted, but further confirmation is needed

elucidate precise pathways. Moreover, long-term toxicity and pharmacokinetic profiles remain unexplored and must be addressed in future animal studies. Further, while the current in silico ADME analysis focused on pharmacokinetic parameters such as absorption potential, solubility, and metabolic stability, future work will include molecular docking studies to identify specific target-ligand interactions relevant to lung cancer treatment. These will involve visualizing binding modes and interaction sequences between curcumin (and other active components of the nanocomposite) and key protein targets such as Bcl-2, EGFR, or caspase-3. Addressing these limitations in subsequent studies will be crucial to advancing the translational potential of these nanomaterials.

Conclusion

This study successfully demonstrated the green synthesis of MgO/Fe_2O_3 NC using *Glycyrrhiza glabra* extract as a natural reducing and capping agent. Functionalization with chitosan and curcumin further enhanced the physicochemical and biological properties of the NC. The synthesized multifunctional nanocomposite exhibited significant antioxidant activity ($IC_{50} = 0.0977$ mg/mL) and significant cytotoxicity toward A549 lung cancer cells ($IC_{50} = 10$ µg/mL) and medium antibacterial activity. Structural and physicochemical characterizations guaranteed stability,

biocompatibility, and crystalline structure of the nanomaterial. To the best of our knowledge, this is the first report that combines *G. glabra*, chitosan, and curcumin in a MgO/Fe_2O_3-based system, where synergistic bioactivity and green synthesis were provided. These findings point toward the promise of this nanocomposite to be a superior candidate for the targeted treatment of lung cancer. In silico ADME analysis supported enhanced cellular uptake and decreased toxicity, reinforcing the formulation's therapeutic potential. Briefly, the findings point to the novel combination of *G. glabra*, chitosan, and curcumin in a MgO/Fe_2O_3 nanoplatform as a green, multifunctional, and biocompatible therapeutic agent for lung cancer therapy. Further in vivo investigations are recommended to validate its therapeutic efficacy and safety.

Acknowledgements This work was funded by Princess Nourah bint Abdulrahman University Researchers Supporting Project Number (PNURSP2025R317), Princess Nourah bint Abdulrahman University, Riyadh, Saudi Arabia.

Author contributions Conceptualization, Alaa Elmetwalli, Ashraf Elsayed, Mohammed S. El-Hersh; experimental work & data analysis, Alaa Elmetwalli, Ashraf Elsayed, Mohammed S. El-Hersh, Mervat G. Hassan, Khaled M. Elattar, Lamia A. Gad, Medhat Ali Salah, Mohamed Basiouny Yahia, Sara Abdelsayed; methodology & investigation, Alaa Elmetwalli, Ashraf Elsayed, Mohammed S. El-Hersh, Mervat G. Hassan, Khaled M. Elattar, Mohamed A. Shaheen, Mohamed F. Ibrahim, Abdullah Mustafa Ibrahim, Hatem Mohamed Newish, Eman Alhomaidi; project administration, Alaa Elmetwalli, Ashraf Elsayed, Mohammed S. El-Hersh, Mervat G. Hassan, Khaled M. Elattar; software, Alaa Elmetwalli, Ashraf Elsayed, Mohammed S. El-Hersh, Mervat G. Hassan, Khaled M. Elattar, Ali H. El-Far; validation Alaa Elmetwalli, Ashraf Elsayed, Mohammed S. El-Hersh, Mervat G. Hassan, Khaled M. Elattar, Eman Alhomaidi; visualization, Alaa Elmetwalli, Ashraf Elsayed, Mohammed S. El-Hersh, Mervat G. Hassan, Khaled M. Elattar; writing—original draft preparation, Alaa Elmetwalli, Khaled M. Elattar, Mohammed S. El-Hersh; writing—review, editing, and provided critical feedback to help shape the research, analysis, and manuscript, Alaa Elmetwalli; All authors have read and agreed to the published version of the manuscript.

Funding No funding.

Data availability Data are provided within the manuscript or supplementary information files.

Declarations

Competing interests The authors declare no competing interests.

Ethics approval and consent to participate Not applicable.

Consent for publication Not applicable.

References

1. Batiha GES, Beshbishy AM, El-Mleeh A, Abdel-Daim MM, Devkota HP. Traditional uses, bioactive chemical constituents, and pharmacological and toxicological activities of *Glycyrrhiza glabra* L. (Fabaceae). Biomolecules. 2020;10(3): 352.
2. Husain I, Bala K, Khan IA, Khan SI. A review on phytochemicals, pharmacological activities, drug interactions, and associated toxicities of licorice (*Glycyrrhiza* sp.). Food Front. 2021;2(4):449–85.
3. Guo L, Katiyo W, Lu L, Zhang X, Wang M, Yan J, Ma X, Yang R, Zou L, Zhao W. Glycyrrhetic acid 3-O-mono-β-d-glucuronide (GAMG): an innovative high-potency sweetener with improved biological activities. Compr Rev Food Sci Food Saf. 2018;17(4):905–19.
4. Ding Y, Brand E, Wang W, Zhao Z. Licorice: resources, applications in ancient and modern times. J Ethnopharmacol. 2022;298: 115594.
5. Ji X, Liu N, Huang S, Zhang C. A comprehensive review of licorice: the preparation, chemical composition, bioactivities and its applications. Am J Chin Med. 2024;52(03):667–716.
6. Yusuf A, Almotairy ARZ, Henidi H, Alshehri OY, Aldughaim MS. Nanoparticles as drug delivery systems: a review of the implication of nanoparticles' physicochemical properties on responses in biological systems. Polymers. 2023;15(7): 1596.
7. Pourmadadi M, Rahmani E, Shamsabadipour A, Mahtabian S, Ahmadi M, Rahdar A, Díez-Pascual AM. Role of iron oxide (Fe_2O_3) nanocomposites in advanced biomedical applications: a state-of-the-art review. Nanomaterials. 2022;12(21): 3873.
8. Batool S, Sohail S, ud Din F, Alamri AH, Alqahtani AS, Alshahrani MA, Alshehri MA, Choi HG. A detailed insight of the tumor targeting using nanocarrier drug delivery system. Drug Deliv. 2023;30(1): 2183815.
9. Mundekkad D, Cho WC. NPs in clinical translation for cancer therapy. Int J Mol Sci. 2022;23(3):1685. https://doi.org/10.3390/ijms23031685.
10. Alqarni LS, Alghamdi MD, Alshahrani AA, Nassar AM. Green nanotechnology: Recent research on bioresource-based NPs synthesis and applications. J Chem. 2022;2022: 4030999. https://doi.org/10.1155/2022/4030999.
11. Haider AJ, Al-Kinani MA, Al-Musawi S. Preparation and characterization of gold coated super paramagnetic iron nanoparticle using pulsed laser ablation in liquid method. Key Eng Mater. 2021;886:77–85. https://doi.org/10.4028/www.scientific.net/KEM.886.77.
12. Abdulwahid FS, Haider AJ, Al-Musawi S. Effect of laser parameter on Fe_3O_4 NPs formation by pulsed laser ablation in liquid. AIP Conf Proc. 2023;2769: 020039. https://doi.org/10.1063/5.0129824.
13 Alnasraui AHF, Joe IH, Al-Musawi S. Design and synthesize of folate decorated Fe_3O_4@ Au-DEX-CP nano formulation for targeted drug delivery in colorectal cancer therapy: *in vitro* and *in vivo* studies. J Drug Deliv Sci Technol. 2023;87: 104798. https://doi.org/10.1016/j.jddst.2023.104798.
14. Althobiti MM, Alzahrani B, Elderdery AY, Alzerwi NA, Rayzah M, Elkhalifa AM, Idrees B, Bakhsh E, Alabdulsalam AA, Mohamedain A, Kumar SS. In vitro anticancer and antimicrobial effects of manganese oxide NPs synthesized using the Glycyrrhiza uralensis leaf extract on breast cancer cell lines. Green Process Synth. 2023;12(1):20230063. https://doi.org/10.1515/gps-2023-0063.
15. Koca FD. Preparation of thymol incorporated organic-inorganic hybrid nanoflowers as a novel fenton agent with intrinsic catalytic and antimicrobial activities. Inorg Nano-Met Chem. 2022;52(2):322–7. https://doi.org/10.1080/24701556.2021.1980024.
16. Ahmad S, Ahmad N, Islam MS, Ahmad MA, Ercisli S, Ullah R, Bari A, Munir I. Rice seeds biofortification using biogenic iron oxide NPs synthesized by using Glycyrrhiza glabra: a study on

growth and yield improvement. Sci Rep. 2024;14(1):12368. https://doi.org/10.1038/s41598-024-62907-1.
17. Koca FD, Duman F. Genotoxic and cytotoxic activity of green synthesized TiO2 NPs. Appl Nanosci. 2019;9:815–23. https://doi.org/10.1007/s13204-018-0712-1.
18. Erdem T, Koca FD. Catalytic and antimicrobial activities of cucumber leaf extract-based organic@ inorganic hybrid nanoflowers through Fenton-like reaction. Rend Lincei Sci Fis Nat. 2023;34(4):1255–61. https://doi.org/10.1007/s12210-023-01206-9.
19. Mundekkad D, Cho WC. Applications of curcumin and its nanoforms in the treatment of cancer. Pharmaceutics. 2023;15(9):2223. https://doi.org/10.3390/pharmaceutics15092223.
20. Kotha RR, Luthria DL. Curcumin: biological, pharmaceutical, nutraceutical, and analytical aspects. Molecules. 2019;24(16):2930. https://doi.org/10.3390/molecules24162930.
21. Rad ME, Egil AC, Ince GO, Yuce M, Zarrabi A. Optimization of curcumin loaded niosomes for drug delivery applications. Colloids Surf A Physicochem Eng Asp. 2022;654: 129921. https://doi.org/10.1016/j.colsurfa.2022.129921.
22. Nambiar S, Osei E, Fleck A, Darko J, Mutsaers AJ, Wettig S. Synthesis of curcumin-functionalized gold NPs and cytotoxicity studies in human prostate cancer cell line. Appl Nanosci. 2018;8:347–57. https://doi.org/10.1007/s13204-018-0728-6.
23. Kuo YC, Wang LJ, Rajesh R. Targeting human brain cancer stem cells by curcumin-loaded NPs grafted with anti-aldehyde dehydrogenase and sialic acid: Colocalization of ALDH and CD44. Mater Sci Eng. 2019;102:362–72. https://doi.org/10.1016/j.msec.2019.04.065.
24. Hammouda MM, Shalabi K, Alanazi AA, Elattar KM, Azzam MA, Rashed MM. Synthesis of novel benzopyrimido[4,5-d] azoninone analogs catalyzed by biosynthesized Ag-TiO2 core/shell magnetic nanocatalyst and assessment of their antioxidant activity. RSC Adv. 2023;13(46):32532–46. https://doi.org/10.1039/D3RA06404B.
25. Allawi F, Juda AM, Radhi SW. Photocatalytic degradation of methylene blue over MgO/α-Fe2O3 nano composite prepared by a hydrothermal method. AIP Conf Proc. 2020. https://doi.org/10.1063/5.0029461.
26. Menazea AA, Ibrahium HA, Awwad NS, Moustapha ME, Farea MO, Bajaber MA. Facile synthesis and high-performance dielectric properties of polyethylene oxide-chitosan-iron oxide NC for electrical applications. J Mater Res Technol. 2022;18:2273–81. https://doi.org/10.1016/j.jmrt.2022.03.058.
27. Farsana NN, MuhideenBadhusha MS, Shakina J, Roshan MM. Synthesis, structural and antimicrobial application of ironoxide/chitosan/curcumin coated NPs. Eur Chem Bull. 2023;12(4):11371–83. https://doi.org/10.48047/ecb/2023.12.si4.1026.
28. Peng S, Sun S. Synthesis and characterization of monodisperse hollow Fe3O4 nanoparticles. Angew Chem Int Ed Engl. 2007;46(22):4155–8.
29. Yao Y, Miao S, Liu S, Ma LP, Sun H, Wang S. Synthesis, characterization, and adsorption properties of magnetic Fe3O4@ graphene nanocomposite. Chem Eng J. 2012;184:326–32.
30. Elmetwalli A, El-Sewedy T, Hassan MG, Abdel-Monem MO, Hassan J, Ismail NF, Salama AF, Fu J, Mousa N, Sabir DK. Gold nanoparticles mediate suppression of angiogenesis and breast cancer growth via MMP-9/NF-κB/mTOR and PD-L1/PD-1 signaling: integrative in vitro validation and network pharmacology insights. Naunyn-Schmiedebergs Arch Pharmacol. 2024. https://doi.org/10.1007/s00210-024-03682-8.
31. Elabd H, Mahboub HH, Salem SM, Abdelwahab AM, Alwutayd KM, Shaalan M, Ismail SH, Abdelfattah AM, Khalid A, Mansour AT, Hamed HS. Nano-curcumin/chitosan modulates growth, biochemical, immune, and antioxidative profiles, and the expression of related genes in Nile tilapia, Oreochromis niloticus. Fishes. 2023;8(7):333. https://doi.org/10.3390/fishes8070333.
32. Ghoniem AA, Elattar KM, Al-Otibi FO, Elsayed A, El-Hersh MS, El-Khateeb AY, Helmy YA, Saber WI. Turmeric extract-mediated biogenic synthesis of Ag@SeO2 magnetic NPs: characterization, optimization, antibacterial and antioxidant activities. RSC Adv. 2024;14(10):7088–111. https://doi.org/10.1039/D4RA00004H.
33. Hammouda MM, Alanazi AA, Elattar KM. Mentha suaveolens leaves extract-mediated synthesis of CoO@TiO2 and Fe2O3@TiO2 Core/Shell NPs with synergistic antimicrobial and antioxidant activities. ChemistrySelect. 2024;9(17): e202401385. https://doi.org/10.1002/slct.202401385.
34. Ghoniem AA, Elattar KM, Alotaibi AS, Ghabban H, El Hersh MS, El-Khateeb AY, El-Amier YA, El-Gendy HM, Eldadamony NM, Saber WI, Elsayed A. Enhanced resistance of Vigna unguiculata to Fusarium oxysporum via Rubia cordifolia extract and growth-promoting endophytic Bacillus amyloliquefaciens DW6. Eur J Plant Pathol. 2024;170(3):567–91. https://doi.org/10.1007/s10658-024-02922-0.
35. Elattar KM, Ghoniem AA, Al-Askar AA, Bhgat El-Gazzar U, El-Hersh MS, Elsherbiny EA, Eldadamony NM, Saber WI. Melanin synthesized by the endophytic aureobasidium pullulans AKW: a multifaceted biomolecule with antioxidant, wound healing, and selective anticancer activity. Curr Top Med Chem. 2024;24(24):2141–60. https://doi.org/10.2174/0115680266300091240730111333.
36. Elattar KM, Al-Otibi FO, El-Hersh MS, Attia AA, Eldadamony NM, Elsayed A, Menaa F, Saber WI. Multifaceted chemical and bioactive features of Ag@ TiO2 and Ag@ SeO2 core/shell nanoparticles biosynthesized using Beta vulgaris L. extract. Heliyon. 2024. https://doi.org/10.1016/j.heliyon.2024.e28359.
37. Alanazi AA, Saber WI, AlDamen MA, Elattar KM. Green synthesis, characterization, and multifunctional applications of Ag@CeO2 and Ag@ CeO2-pullulan nanocomposites for dye degradation, antioxidant, and antifungal activities. Int J Biol Macromol. 2024;280: 135862.
38. Eldadamony NM, Ghoniem AA, Al-Askar AA, Attia AA, El-Hersh MS, Elattar KM, Alrdahi H, Saber WI. Optimization of pullulan production by Aureobasidium pullulans using semi-solid-state fermentation and artificial neural networks: characterization and antibacterial activity of pullulan impregnated with Ag-TiO2 nanocomposite. Int J Biol Macromol. 2024;269: 132109.
39. Boyanova L, Gergova G, Nikolov R, Derejian S, Lazarova E, Katsarov N, Mitov I, Krastev Z. Activity of Bulgarian propolis against 94 Helicobacter pylori strains in vitro by agar-well diffusion, agar dilution and disc diffusion methods. J Med Microbiol. 2005;54(5):481–3.
40. Hassan MG, Hamed AA, Elmetwalli A, Abdel-Monem MO, El-Shora HM, Alsallami WM. Assessment of myco-fabricated Al2O3 NPs toxicity on cancer cells and pathogenic microbes by suppression of bacterial metabolic key enzymes. Int J Biol Macromol. 2024;283: 137073.
41. Elmetwalli A, Abdel-Monem MO, El-Far AH, Ghaith GS, Albalawi NAN, Hassan J, Ismail NF, El-Sewedy T, Alnamshan MM, ALaqeel NK. Probiotic-derived silver nanoparticles target mTOR/MMP-9/BCL-2/dependent AMPK activation for hepatic cancer treatment. Med Oncol. 2024;41(5): 106.
42. Al Balawi AN, Eldiasty JG, Mosallam SAER, El-Alosey AR, Elmetwalli A. Assessing multi-target antiviral and antioxidant activities of natural compounds against SARS-CoV-2: an integrated in vitro and in silico study. Bioresour Bioprocess. 2024;11(1):108.

43. Hassan MG, Farouk HS, Baraka DM, Khedr M, El Awady ME, Ameen F, Sajjad Z, Elmetwalli A. Pomegranate's silver bullet: nature-powered nanoparticles deliver a one-two punch against cancer and antimicrobial resistance. Inorg Chem Commun. 2024;168: 112853.
44. Cerulli A, Masullo M, Montoro P, Piacente S. Licorice (Glycyrrhiza glabra, G. uralensis, and G. inflata) and their constituents as active cosmeceutical ingredients. Cosmet. 2022;9(1): 7.
45. McSkimming A, Colbran SB. The coordination chemistry of organo-hydride donors: new prospects for efficient multi-electron reduction. Chem Soc Rev. 2013;42(12):5439–88. https://doi.org/10.1039/c3cs35466k.
46. He MQ, Ai Y, Hu W, Guan L, Ding M, Liang Q. Recent advances of seed-mediated growth of metal NPs: from growth to applications. Adv Mater. 2023;35(46): 2211915. https://doi.org/10.1002/adma.202211915.
47. Niederberger M, Garnweitner G. Organic reaction pathways in the nonaqueous synthesis of metal oxide nanoparticles. Chem Eur J. 2006;12(28):7282–302.
48. Restrepo CV, Villa CC. Synthesis of silver NPs, influence of capping agents, and dependence on size and shape: a review. Environ Nanotechnol Monit Manag. 2021;15: 100428. https://doi.org/10.1016/j.enmm.2021.100428.
49. Zhu C, Liu F, Zhang Y, Wei M, Zhang X, Ling C, Li A. Nitrogen-doped chitosan-Fe (III) composite as a dual-functional material for synergistically enhanced co-removal of Cu (II) and Cr (VI) based on adsorption and redox. Chem Eng J. 2016;306:579–87. https://doi.org/10.1016/j.cej.2016.07.096.
50. Bhattarai SR, Kc RB, Aryal S, Khil MS, Kim HY. N-acylated chitosan stabilized iron oxide NPs as a novel nano-matrix and ceramic modification. Carbohydr Polym. 2007;69(3):467–77. https://doi.org/10.1016/j.carbpol.2007.01.006.
51. Mekahlia S, Bouzid B. Chitosan-copper (II) complex as antibacterial agent: synthesis, characterization and coordinating bond-activity correlation study. Phys Procedia. 2009;2(3):1045–53. https://doi.org/10.1016/j.phpro.2009.11.061.
52. Murugesan S, Scheibel T. Chitosan-based NC for medical applications. J Polym Sci. 2021;59(15):1610–42. https://doi.org/10.1002/pol.20210251.
53. Ali A, Ahmed S. A review on chitosan and its NC in drug delivery. Int J Biol Macromol. 2018;109:273–86. https://doi.org/10.1016/j.ijbiomac.2017.12.078.
54. Wang N, Fan H, Wang J, Wang H, Liu T. Fabrication and characterization of curcumin-loaded composite NPs based on high-hydrostatic-pressure-treated zein and pectin: interaction mechanism, stability, and bioaccessibility. Food Chem. 2024;446: 138286. https://doi.org/10.1016/j.foodchem.2023.138286.
55. Li S, Mu B, Yan P, Kang Y, Wang Q, Wang A. Incorporation of different metal ion for tuning color and enhancing antioxidant activity of curcumin/palygorskite hybrid materials. Front Chem. 2021;9: 760941. https://doi.org/10.3389/fchem.2021.760941.
56. Rafiee Z, Nejatian M, Daeihamed M, Jafari SM. Application of different nanocarriers for encapsulation of curcumin. Crit Rev Food Sci Nutr. 2019;59(21):3468–97. https://doi.org/10.1080/10408398.2018.1495174.
57. Tonga M, Lahti PM. Designing conjugation-extended viologens for high molar absorptivity with longer wavelength absorption. Synth Met. 2019;254:75–84. https://doi.org/10.1016/j.synthmet.2019.06.003.
58. Singh V, Mishra AK. White light emission from a mixture of pomegranate extract and carbon NPs obtained from the extract. J Mater Chem C. 2016;4(15):3131–7. https://doi.org/10.1039/C6TC00480F.
59. Lu H, Mack J, Yang Y, Shen Z. Structural modification strategies for the rational design of red/NIR region BODIPYs. Chem Soc Rev. 2014;43(13):4778–823. https://doi.org/10.1039/C4CS00030G.
60. Elfadl AA, Bashal AH, Habeeb TH, Khalafalla MA, Alkayal NS, Khalil KD. Preparation, characterization, dielectric properties, and AC conductivity of chitosan stabilized metallic oxides CoO and SrO: experiments and tight binding calculations. Polymers. 2023;15(20):4132. https://doi.org/10.3390/polym15204132.
61. Basumallick S. Synthesis and study of chemo-hydrothermally derived water-soluble chitosan and chiosan-metal oxide composites. Orlando: University of Central Florida; 2014.
62. Jaiswal VD, Dongre PM. Biophysical interactions between silver NPs-albumin interface and curcumin. J Pharm Anal. 2020;10(2):164–77. https://doi.org/10.1016/j.jpha.2020.02.004.
63. Sharma A, Singh BP, Dhar S, Gondorf A, Spasova M. Effect of surface groups on the luminescence property of ZnO NPs synthesized by sol–gel route. Surf Sci. 2012;606(3–4):L13–7. https://doi.org/10.1016/j.susc.2011.09.006.
64. Zuo X, Wang X, Si G, Zhang D, Yu X, Guo Z, Gu N. Size-dependent oxygen vacancy of iron oxide NPs. Small Methods. 2024. https://doi.org/10.1002/smtd.202400685.
65. Branca C, D'Angelo G, Crupi C, Khouzami K, Rifici S, Ruello G, Wanderlingh U. Role of the OH and NH vibrational groups in polysaccharide-NC interactions: a FTIR-ATR study on chitosan and chitosan/clay films. Polymer. 2016;99:614–22. https://doi.org/10.1016/j.polymer.2016.07.086.
66. Bharathi D, Ranjithkumar R, Vasantharaj S, Chandarshekar B, Bhuvaneshwari V. Synthesis and characterization of chitosan/iron oxide NC for biomedical applications. Int J Biol Macromol. 2019;132:880–7. https://doi.org/10.1016/j.ijbiomac.2019.03.233.
67. Utaiyachandran M, Durairaj K, Kumar AJ, Sivakumar S, Palanivel V, Senthilkumar P. Photo-assisted assembly of MgO/Fe2O3 composites for photocatalytic Rhodamine B degradation and their mimicking activity. Desalin Water Treat. 2023;314:263–75. https://doi.org/10.5004/dwt.2023.30110.
68. Ghdeeb NJ, AbdulMajeed AM, Mohammed AH. Role of extracted nano-metal oxides from factory wastes in medical applications. Iraqi J Sci. 2023. https://doi.org/10.24996/ijs.2023.64.4.12.
69. Serrano-Lotina A, Portela R, Baeza P, Alcolea-Rodríguez V, Villarroel M, Ávila P. Zeta potential as a tool for functional materials development. Catal Today. 2023;423:113862. https://doi.org/10.1016/j.cattod.2022.08.004.
70. Hurwitz G, Guillen GR, Hoek EM. Probing polyamide membrane surface charge, zeta potential, wettability, and hydrophilicity with contact angle measurements. J Membr Sci. 2010;349(1–2):349–57. https://doi.org/10.1016/j.memsci.2009.11.063.
71. Leroy P, Tournassat C, Bizi M. Influence of surface conductivity on the apparent zeta potential of TiO2 NPs. J Colloid Interface Sci. 2011;356(2):442–53. https://doi.org/10.1016/j.jcis.2011.01.016.
72. Diodati S, Dolcet P, Casarin M, Gross S. Pursuing the crystallization of mono-and polymetallic nanosized crystalline inorganic compounds by low-temperature wet-chemistry and colloidal routes. Chem Rev. 2015;115(20):11449–502. https://doi.org/10.1021/acs.chemrev.5b00275.
73. Khezri A, Karimi A, Yazdian F, Jokar M, Mofradnia SR, Rashedi H, Tavakoli Z. Molecular dynamic of curcumin/chitosan interaction using a computational molecular approach: emphasis on biofilm reduction. Int J Biol Macromol. 2018;114:972–8. https://doi.org/10.1016/j.ijbiomac.2018.03.100.
74. Gokce Y, Cengiz B, Yildiz N, Calimli A, Aktas Z. Ultrasonication of chitosan NPs suspension: influence on particle size. Colloids Surf A Physicochem Eng Asp. 2014;462:75–81. https://doi.org/10.1016/j.colsurfa.2014.08.028.
75. Xu P, Qian Y, Wang R, Chen Z, Wang T. Entrapping curcumin in the hydrophobic reservoir of rice proteins toward stable

antioxidant NPs. Food Chem. 2022;387: 132906. https://doi.org/10.1016/j.foodchem.2022.132906.
76. Tyukova IS, Safronov AP, Kotel'Nikova AP, Agalakova DY. Electrostatic and steric mechanisms of iron oxide NPs sol stabilization by chitosan. Polym Sci Ser A. 2014;56:498–504. https://doi.org/10.1134/S0965545X14040178.
77. Chouhan D, Mandal P. Applications of chitosan and chitosan based metallic NPs in agrosciences-a review. Int J Biol Macromol. 2021;166:1554–69. https://doi.org/10.1016/j.ijbiomac.2020.11.035.
78. Dong C, Chen W, Liu C, Liu Y, Liu H. Synthesis of magnetic chitosan NPs and its adsorption property for humic acid from aqueous solution. Colloids Surf A Physicochem Eng Asp. 2014;446:179–89. https://doi.org/10.1016/j.colsurfa.2014.01.069.
79. Wang J, Zhuang S. Chitosan-based materials: preparation, modification and application. J Clean Prod. 2022;355: 131825. https://doi.org/10.1016/j.jclepro.2022.131825.
80. Mukhopadhyay P, Mishra R, Rana D, Kundu PP. Strategies for effective oral insulin delivery with modified chitosan NPs: a review. Prog Polym Sci. 2012;37(11):1457–75. https://doi.org/10.1016/j.progpolymsci.2012.04.004.
81. Hadi Z, Nouraliei M, Yousefi-Siavoshani A, Javadian H, Chalanchi SM, Hashemi SS. A DFT study on the therapeutic potential of carbon nanostructures as sensors and drug delivery carriers for curcumin molecule: NBO and QTAIM analyses. Colloids Surf A Physicochem Eng Asp. 2022;651: 129698. https://doi.org/10.1016/j.colsurfa.2022.129698.
82. Lee WH, Loo CY, Rohanizadeh R. Functionalizing the surface of hydroxyapatite drug carrier with carboxylic acid groups to modulate the loading and release of curcumin NPs. Mater Sci Eng. 2019;99:929–39. https://doi.org/10.1016/j.msec.2019.02.030.
83. Baruah K, Singh AK, Kumari K, Nongbri DL, Jha AN, Singha Roy A. Interactions of turmeric-and curcumin-functionalized gold nanoparticles with human serum albumin: exploration of protein corona formation, binding, thermodynamics, and antifibrillation studies. Langmuir. 2023;40(2):1381–98.
84. Hu Q, Luo Y. Chitosan-based nanocarriers for encapsulation and delivery of curcumin: a review. Int J Biol Macromol. 2021;179:125–35.
85. Guo Y-F, Guo X-M. Formation of [Mg1-x, Fex] O· Fe2O3 in solid-state reactions between MgO and Fe2O3 in the Fe2O3-rich system. ISIJ Int. 2017;57(2):228–35.
86. Kumar R, Prakash K, Cheang P, Gower L, Khor K. Chitosan-mediated crystallization and assembly of hydroxyapatite nanoparticles into hybrid nanostructured films. J R Soc Interface. 2008;5(21):427–39.
87. Zhang Y, Sun X. Photocatalytic degradation of dyes using ferrite nanoparticles. J Environ Chem Eng. 2019;7(3): 103162. https://doi.org/10.1016/j.jece.2019.103162.
88. Kumar KV, Ramisetty KA, Devi KR, Krishna GR, Heffernan C, Stewart AA, Guo J, Gadipelli S, Brett DJ, Favvas EP. Pure curcumin spherulites from impure solutions via nonclassical crystallization. ACS Omega. 2021;6(37):23884–900.
89. Yang B, Dong Y, Wang F, Zhang Y. Nanoformulations to enhance the bioavailability and physiological functions of polyphenols. Molecules. 2020;25(20):4613.
90. Soraki RK, Gerami M, Ramezani M. Effect of graphene/metal nanocomposites on the key genes involved in rosmarinic acid biosynthesis pathway and its accumulation in Melissa officinalis. BMC Plant Biol. 2021;21(1):260.
91. Wen J, Salunke BK, Kim BS. Biosynthesis of graphene-metal nanocomposites using plant extract and their biological activities. J Chem Technol Biotechnol. 2017;92(6):1428–35.
92. Rezagholizade-shirvan A, Najafi MF, Behmadi H, Masrournia M. Preparation of nano-composites based on curcumin/chitosan-PVA-alginate to improve stability, antioxidant, antibacterial and anticancer activity of curcumin. Inorg Chem Commun. 2022;145: 110022.
93. Wright JS. Predicting the antioxidant activity of curcumin and curcuminoids. J Mol Struct. 2002;591(1–3):207–17.
94. Aranaz I, Mengibar M, Harris R, Paños I, Miralles B, Acosta N, Galed G, Heras Á. Functional characterization of chitin and chitosan. Curr Chem Biol. 2009;3(2):203–30.
95. Fozi V, Esmaeili H, Alizadeh A, Eghlima G, Mirjalili MH. The interaction effect of water deficit stress and seaweed extract on phytochemical characteristics and antioxidant activity of licorice (*Glycyrrhiza glabra L.*). Front Plant Sci. 2024;15: 1474399.
96. Nie Z, Liu KJ, Zhong C-J, Wang L-F, Yang Y, Tian Q, Liu Y. Enhanced radical scavenging activity by antioxidant-functionalized gold nanoparticles: a novel inspiration for development of new artificial antioxidants. Free Radic Biol Med. 2007;43(9):1243–54.
97. Heidari G, Hassanpour M, Nejaddehbashi F, Sarfjoo MR, Yousefiasl S, Sharifi E, Bigham A, Agarwal T, Borzacchiello A, Lagreca E. Biosynthesized nanomaterials with antioxidant and antimicrobial properties. Mater Chem Horiz. 2022;1(1):35–48.
98. Draviana HT, Fitriannisa I, Khafid M, Krisnawati DI, Widodo, Lai C-H, Fan Y-J, Kuo T-R. Size and charge effects of metal nanoclusters on antibacterial mechanisms. J Nanobiotechnol. 2023;21(1):428.
99. Wang S, Meckling KA, Marcone MF, Kakuda Y, Tsao R. Synergistic, additive, and antagonistic effects of food mixtures on total antioxidant capacities. J Agric Food Chem. 2011;59(3):960–8.
100. Alizadeh N, Malakzadeh S. Antioxidant, antibacterial and anticancer activities of β-and γ-CDs/curcumin loaded in chitosan NPs. Int J Biol Macromol. 2020;147:778–91. https://doi.org/10.1016/j.ijbiomac.2020.01.206.
101. Targhi AA, Moammeri A, Jamshidifar E, Abbaspour K, Sadeghi S, Lamakani L, Akbarzadeh I. Synergistic effect of curcumin-Cu and curcumin-Ag NPs loaded niosome: enhanced antibacterial and anti-biofilm activities. Bioorg Chem. 2021;115: 105116. https://doi.org/10.1016/j.bioorg.2021.105116.
102. Das B, Dash SK, Mandal D, Ghosh T, Chattopadhyay S, Tripathy S, Das S, Dey SK, Das D, Roy S. Green synthesized silver NPs destroy multidrug resistant bacteria via reactive oxygen species mediated membrane damage. Arab J Chem. 2017;10(6):862–76. https://doi.org/10.1016/j.arabjc.2015.08.008.
103. Ejaz S, Ejaz S, Shahid R, Noor T, Shabbir S, Imran M. Chitosan-curcumin complexation to develop functionalized nanosystems with enhanced antimicrobial activity against hetero-resistant gastric pathogen. Int J Biol Macromol. 2022;204:540–54. https://doi.org/10.1016/j.ijbiomac.2022.02.039.
104. Tang S, Zheng J. Antibacterial activity of silver NPs: structural effects. Adv Healthc Mater. 2018;7(13):1701503. https://doi.org/10.1002/adhm.201701503.
105. Doostmohammadi A, Jooya H, Ghorbanian K, Gohari S, Dadashpour M. Potentials and future perspectives of multi-target drugs in cancer treatment: the next generation anti-cancer agents. Cell Commun Signal. 2024;22(1):228. https://doi.org/10.1186/s12964-024-01607-9.
106. Kamalipooya S, Fahimirad S, Abtahi H, Golmohammadi M, Satari M, Dadashpour M, Nasrabadi D. Diabetic wound healing function of PCL/cellulose acetate nanofiber engineered with chitosan/cerium oxide nanoparticles. Int J Pharm. 2024;653: 123880. https://doi.org/10.1016/j.ijpharm.2024.123880.
107. Serati-Nouri H, Rasoulpoor S, Pourpirali R, Sadeghi-Soureh S, Esmaeilizadeh N, Dadashpour M, Roshangar L, Zarghami N. In vitro expansion of human adipose-derived stem cells with delayed senescence through dual stage release of curcumin from

mesoporous silica nanoparticles/electrospun nanofibers. Life Sci. 2021;285: 119947. https://doi.org/10.1016/j.lfs.2021.119947.
108. Anand P, Kunnumakkara AB, Newman RA, Aggarwal BB. Bioavailability of curcumin: problems and promises. Mol Pharm. 2007;4(6):807–18. https://doi.org/10.1021/mp700113r.
109. Prabaharan M. Review paper: chitosan derivatives as promising materials for controlled drug delivery. J Biomater Appl. 2008;23(1):5–36. https://doi.org/10.1177/0885328208091562.
110. Lôbo GC, Paiva KL, Silva ALG, Simões MM, Radicchi MA, Báo SN. Nanocarriers used in drug delivery to enhance immune system in cancer therapy. Pharmaceutics. 2021;13(8):1167. https://doi.org/10.3390/pharmaceutics13081167.
111. Li Y, Li N, Jiang W, Ma G, Zangeneh MM. In situ decorated Au NPs on pectin-modified Fe3O4 NPs as a novel magnetic nanocomposite (Fe3O4/pectin/Au) for catalytic reduction of nitroarenes and investigation of its anti-human lung cancer activities. Int J Biol Macromol. 2020;163:2162–71.
112. Sharifi-Azad M, Fathi M, Cho WC, Barzegari A, Dadashi H, Dadashpour M, Jahanban-Esfahlan R. Recent advances in targeted drug delivery systems for resistant colorectal cancer. Cancer Cell Int. 2022;22(1):196. https://doi.org/10.1186/s12935-022-02605-y.
113. Azar LK, Dadashpour M, Hashemi M, Zarghami N. Design and development of nanostructured co-delivery of artemisinin and chrysin for targeting hTERT gene expression in breast cancer cell line: possible clinical application in cancer treatment. Asian Pac J Cancer Prev. 2022. https://doi.org/10.31557/APJCP.2022.23.3.919.
114. Aggarwal BB, Kumar A, Bharti AC. Anticancer potential of curcumin: preclinical and clinical studies. Anticancer Res. 2003;23(1A):363–98.
115. Noor A, Shafi S, Sehar N, Qadir I, Rashid S, Arafah A, Rehman MU. Curcuminoids as cell signaling pathway modulators: a potential strategy for cancer prevention. Curr Med Chem. 2024;31(21):3093–117. https://doi.org/10.2174/0929867331666230809100335.
116. Nayak D, Minz AP, Ashe S, Rauta PR, Kumari M, Chopra P, Nayak B. Synergistic combination of antioxidants, silver NPs and chitosan in a NPs based formulation: characterization and cytotoxic effect on MCF-7 breast cancer cell lines. J Colloid Interface Sci. 2016;470:142–52. https://doi.org/10.1016/j.jcis.2016.02.043.
117. Bai J, Gongsun X, Xue L, Zangeneh MM. Introducing a modern chemotherapeutic drug formulated by iron nanoparticles for the treatment of human lung cancer. J Exp Nanosci. 2021;16(1):397–409.
118. Mahjoubin-Tehran M, Rezaei S, Kesharwani P, Sahebkar A. Nanospheres for curcumin delivery as a precision nanomedicine in cancer therapy. J Biomater Sci Polym Ed. 2024. https://doi.org/10.1080/09205063.2024.2371186.
119. Shi Z, Mahdavian Y, Mahdavian Y, Mahdigholizad S, Irani P, Karimian M, Abbasi N, Ghaneialvar H, Zangeneh A, Zangeneh MM. Cu immobilized on chitosan-modified iron oxide magnetic nanoparticles: preparation, characterization and investigation of its anti-lung cancer effects. Arab J Chem. 2021;14(8): 103224.
120. Gabr SA, et al. Curcumin modulates oxidative stress, fibrosis, and apoptosis in drug-resistant cancer cell lines. Life. 2022;12(9):1427.
121. Seyed MA, et al. A comprehensive review on the chemotherapeutic potential of piceatannol for cancer treatment, with mechanistic insights. J Agric Food Chem. 2016;64(4):725–37.
122. Elmetwalli A, et al. Nanoparticle zinc oxide obviates oxidative stress of liver cells in induced-diabetes mellitus model. Med J Viral Hepat. 2022;7(1):8–12.
123. Elattar KM, et al. Green-synthesized silver–copper nanocomposites from Sargassum latifolium: antibacterial, anticancer, and in silico pharmacokinetic evaluation. Med Oncol. 2025. https://doi.org/10.1007/s12032-025-02899-8.
124. Elhabal SF, et al. Green synthesis of zinc oxide nanoparticles from *althaea officinalis* flower extract coated with chitosan for potential healing effects on diabetic wounds by inhibiting TNF-α and IL-6/IL-1β signaling pathways. Int J Nanomed. 2024. https://doi.org/10.2147/IJN.S455270.

Authors and Affiliations

Alaa Elmetwalli[1] · Sara Abdelsayed[2] · Ashraf Elsayed[3] · Mohammed S. El-Hersh[4] · Mervat G. Hassan[2] · Lamia A. Gad[5] · Medhat Ali Salah[6] · Mohamed Basiouny Yahia[6] · Mohamed A. Shaheen[6] · Mohamed F. Ibrahim[6] · Abdullah Mustafa Ibrahim[6] · Hatem Mohamed Newish[7] · Eman Alhomaidi[8] · Ali H. El-Far[9] · Khaled M. Elattar[10]

✉ Alaa Elmetwalli
aelmetwalli@ut.edu.sa; dr.prof2011@gmail.com

✉ Ashraf Elsayed
Ashraf-badawy@mans.edu.eg

1 Prince Fahad bin Sultan Research Chair for Biomedical Research, University of Tabuk, Tabuk, Saudi Arabia

2 Department of Botany and Microbiology, Faculty of Science, Benha University, Benha, Egypt

3 Botany Department, Faculty of Science, Mansoura University, Elgomhouria St, Mansoura 35516, Egypt

4 Microbial Activity Unit, Department of Microbiology, Soils, Water and Environment Research Institute, Agricultural Research Center, Giza 12619, Egypt

5 Clinical Pathology, Faculty of Medicine for Girls, Al-Azhar University, Cairo, Egypt

6 Clinical Pathology, Faculty of Medicine for Boys, Al-Azhar University, Cairo, Egypt

7 Medical Microbiology and Immunology Department, Faculty of Medicine, Al-Azhar University, Cairo, Egypt

8 Department of Biology, College of Science, Princess Nourah bint Abdulrahman University, 11671 Riyadh, Saudi Arabia

[9] Key Laboratory of Epigenetics and Oncology, The Research Center for Preclinical Medicine, Southwest Medical University, Luzhou 646000, China

[10] Unit of Genetic Engineering and Biotechnology, Mansoura University, El-Gomhoria Street, Mansoura 35516, Egypt